FEDERAL UNIVERSITY OF AMAZONAS

GRADUATE PROGRAM IN PHYSICS

Head-to-Tail and Head-to-Head Molecular Chains of Poly(*p*-anisidine): Combined Experimental and Theoretical Evaluation

LILIAN RODRIGUES DE OLIVEIRA

Manaus/AM

September, 2022

LILIAN RODRIGUES DE OLIVEIRA

Head-to-Tail and Head-to-Head Molecular Chains of Poly(*p*-anisidine): Combined Experimental and Theoretical Evaluation

Thesis submitted in fulfillment of the requirements for the Degree of Doctor in Physics.

Advisor: Prof. Dr. Edgar Aparecido Sanches

Manaus/AM

September, 2022

Ficha Catalográfica

Ficha catalográfica elaborada automaticamente de acordo com os dados fornecidos pelo(a) autor(a).

O48h

Oliveira, Lilian Rodrigues de
Head-to-tail and head-to-head molecular chains of poly(p-anisidine): combined experimental and theoretical evaluation / Lilian Rodrigues de Oliveira . 2022
87 f.: il. color; 31 cm.

Orientador: Edgar Aparecido Sanches
Tese (Física) - Universidade Federal do Amazonas.

1. poly(p–anisidine). 2. conjugated polymer. 3. dft. 4. head-to-tail. 5. multifractal analysis. I. Sanches, Edgar Aparecido. II. Universidade Federal do Amazonas III. Título

““Eye has not seen, nor ear heard,
Nor have entered into the heart of man
The things which God has prepared for those who love Him.”
1 Corinthians 2:9

ACKNOWLEDGMENTS

- To **God** for allowing the development of this work and for all the achievements that have brought me here.
- To my mother, **Maria Olinda Alvarado Rodrigues**, for her love and friendship, for all the support she has given me during my academic journey, always encouraging and doing everything in her power for my studies. My victory is your victory. Love you!
- To my father, **Luciano José de Oliveira**, for all the help and support throughout this journey.
- To my husband, **Edieliton Oliveira**, for taking care of me with so much love, for the partnership and companionship that have lasted almost 11 years. Our love multiplied and we inherited our son Joaquim, who will soon be in our arms. Thank you for everything, my love, I love you. I love our family!
- To my advisor **Prof. Dr. Edgar Aparecido Sanches**, thank you so much for everything, especially for your patience and understanding during this period. It would not have been possible to complete this work without your contribution, support, and permanent help. I will always be grateful for everything you've done for me. Your success is the result of your tireless and brilliant work.
- To my family **Renata**, **Adalmir**, **Estevânia** and **Edilson**, for all encouragement and motivation.
- To my family at heart, made up of my dear friends, **Katrine**, **Bruna**, **Orlando**, **Alessandra**, **Marcos**, **Davi**, **Carlos Alberto**, **Carol**, **Neto**, **Lin**, **Rafaela**, **Yohei**, **Marcelli**, **Ana**, **Rafael**, **Adriane**, **Daniela** and **Lucas**. You are a treasure God has given me.
- To my pets Belinha, Madalena, Christian Grey, Pêto and Perequetucha. Thank you for making my days even happier. In particular, to our cat Madox who this year became a little star. Edi and I will always love and miss you.
- To my PhD colleagues, whom I had the great pleasure of working with, **Cleverton**, **Cláudio**, **Thainnar**, **Adriano** and **Douglas**. You are from the galaxies!!!
- To my dear friends and coworkers from NANOPOL who provided a motivating, collaborative, and laughing work environment: **Adriano Carolino**, **Ana Luisa**, **Ronald Aguiar** e **Matheus Biondo**.
- To **Douglas Gonçalves**, who patiently guided me and taught me everything I needed to learn about computer simulation. Without your instructions everything would have been more difficult. Thank you for all your help and immense contribution.
- To Laboratory of Nanostructured Polymers – NANOPOL, for the infrastructure and welcoming working environment.
- To **LabMat (UFAM)** and **LPMat (UFAM)** for the performed analyzes of X-ray Diffraction and Complex Impedance Spectroscopy measurements.
- To Professor **Angsula Ghosh**, for her willingness to help and open doors throughout my postgraduate period.
- To Professor **William Marcondes**, for the interpretation of the NMR measurements, which were considerably important in this study. Thank you for clarifying and discussing each point.
- To the Fundação de Amparo à Pesquisa do Estado do Amazonas (FAPEAM), for the Doctoral scholarship granted (process 062.00478/2019).

ABSTRACT

Poly(*p*–anisidine) (PPA) is a polyaniline presenting a methoxy (–OCH_3) group at the *para* position of the phenyl ring. Considering the important role of conjugated polymers in novel technological applications, a systematic, combined experimental and theoretical investigation had been performed to get more insight into the crystallization process of PPA. Conventional oxidative polymerization of *p*–anisidine monomer was based on a Central Composite Rotational Design (CCRD). The effect of the concentration of the monomer, ammonium persulfate (APS) and HCl on the percentage of crystallinity was considered. Several experimental techniques such as X-Ray diffraction (XRD), Scanning Electron Microscopy (SEM), Multifractal Analysis, Nuclear Magnetic Resonance (^{13}C NMR), Fourier-transform Infrared Spectroscopy (FTIR), Complex Impedance Spectroscopy analysis besides Density Functional Theory (DFT) were employed to perform a systematic investigation of PPA. The experimental treatments resulted in different crystal structures with the percentage of crystallinity ranging from (29.2 ± 0.6) % ($PPA1_{HT}$) to (55.1 ± 0.2) % ($PPA16_{HT\text{-}HH}$). The XRD patterns of $PPA1_{HT}$ and $PPA16_{HT\text{-}HH}$ were clearly correlated, but more defined in $PPA1_{HT}$. A broad hallo in the $PPA16_{HT\text{-}HH}$ pattern from 2θ = 10.0° – 30.0° suggested reduced crystallinity. Basically, two types of morphology were observed in both samples: needles and globular particles. SEM images suggested that the needles morphology might be related to the crystalline contribution. Multifractal analysis showed that the PPA surface became more irregular and complex when the crystallinity was reduced. The proposed molecular structures of PPA were supported by the high-resolution ^{13}C NMR results, allowing to access the percentage of head–to–tail (HT) and head–to–head (HH) molecular structures: $PPA1_{HT}$ was fully (100%) constituted of HT polymer chains (PPA_{HT}), while PPA16 was formed predominantly by HT molecular structure [(62.0 ± 0.5) %; $PPA_{HT\text{-}HH}$). Comparing calculated and experimental FTIR spectra, the most pronounced changes were observed in ν(C–H), ν(N–H), ν(C–O) and ν(C–N–C) due to the influence of counter ions, as well as by the different mechanisms of polymerization. Finally, a significant difference in electrical conductivity values was observed in the range of 1.00×10^{-9} $S.cm^{-1}$ and 3.90×10^{-14} $S.cm^{-1}$, respectively, for $PPA1_{HT}$ and $PPA16_{HT\text{-}HH}$.

Keywords: poly(*p*–anisidine), conjugated polymer, DFT, head-to-tail, head-to-head, multifractal analysis.

RESUMO

A poli(*p*–anisidina) (PPA) é uma polianilina que apresenta um grupo metoxi (–OCH_3) na posição *para* do anel fenil. Considerando o importante papel dos polímeros conjugados em aplicações tecnológicas, uma investigação sistemática combinando dados experimentais e teóricos foi realizada para obter mais informações sobre o processo de cristalização da PPA. A polimerização oxidativa convencional do monômero *p*-anisidina foi baseada em um projeto rotacional composto central (CCRD). Foi considerado o efeito da concentração do monômero, persulfato de amônio (APS) e HCl no percentual de cristalinidade. Técnicas experimentais como Difração de Raios X (DRX), Microscopia Eletrônica de Varredura (MEV), Análise Multifractal, Ressonância Magnética Nuclear (RMN ^{13}C), Espectroscopia no Infravermelho por Transformada de Fourier (FTIR), Espectroscopia de Impedância Complexa, além da Teoria do Funcional da Densidade (DFT) foram empregados para realizar uma investigação sistemática da PPA. Os tratamentos experimentais resultaram em diferentes estruturas cristalinas com porcentual de cristalinidade variando de (29,2 ± 0,6) % ($PPA1_{HT}$) a (55,1 ± 0,2) % ($PPA16_{HT\text{-}HH}$). Os padrões de DRX de $PPA1_{HT}$ e $PPA16_{HT\text{-}HH}$ foram claramente correlacionados, mas mais definidos para $PPA1_{HT}$. Um amplo halo no padrão da $PPA16_{HT\text{-}HH}$ de 2θ = 10,0° – 30,0° sugeriu cristalinidade reduzida. Basicamente, dois tipos de morfologia foram observados em ambas as amostras: agulhas e partículas globulares. As imagens de MEV sugeriram que a morfologia das agulhas pode estar relacionada com a contribuição cristalina. A análise multifractal mostrou que a superfície do PPA se tornou mais irregular e complexa quando a cristalinidade foi reduzida. As estruturas moleculares propostas da PPA foram correlacionadas com os resultados de RMN ^{13}C de alta resolução, permitindo acessar o percentual de estruturas moleculares cabeça-cauda (HT) e cabeça-cabeça (HH): $PPA1_{HT}$ foi totalmente (100%) constituída por cadeias poliméricas HT, enquanto a PPA16 foi formada predominantemente por estrutura molecular HT [(62,0 ± 0,5) %. Comparando os espectros de FTIR calculados e experimentais, as mudanças mais pronunciadas foram observadas em ν(C–H), ν(N–H), ν(C–O) e ν(C–N–C) devido à influência dos contra-íons dopantes, bem como pelos diferentes mecanismos de polimerização. Por fim, foi observada uma diferença significativa nos valores de condutividade elétrica na faixa de $1,00 \times 10^{-9}$ e $3,90 \times 10^{-14}$ $S.cm^{-1}$, respectivamente, para $PPA1_{HT}$ e $PPA16_{HT\text{-}HH}$.

Palavras-chave: poli(*p*–anisidina), polímero conjugado, DFT, cabeça-cauda, cabeça-cabeça, análise multifractal.

LIST OF FIGURES

LIST OF TABLES

SUMÁRIO

1. INTRODUCTION

The polyconjugated structure of Intrinsically Conducting Polymers (ICP) plays an important role mainly on their crystal structure and electrical properties [1–3]. Some advantages of conjugated polymers are based on their methods of synthesis [4] and good environmental stability, allowing the development of emerging materials [5–7].

Structural aspects in polyanilines continue to be an interesting research topic [8–10]. Efforts have been devoted to improve their crystallinity, processability and electrical conductivity by using appropriate functionalized protonic acids, novel mechanisms of polymerization, as well as substituted polyanilines [1,2,4,11]. Polyaniline derivatives are based on a suitable substituent attached either at the nitrogen atom or in the phenyl ring of the repeated unit [2,12–14]. Anisidine is an aromatic amine (methoxyaniline) present in three isomeric forms: *ortho*–, *meta*–, and *para*–anisidine.

The electronic characteristics of aniline derivatives is based on the aniline ring substitutions [15]. Among the substituted polyaniline derivatives, poly(*p*-anisidine) (PPA) is a polyaniline presenting a methoxy (–OCH_3) group at the *para* position of the phenyl ring [16–18]. The electron-donating substituent groups at the aromatic rings strongly influences the conformational modifications of conjugated polymers [2] allowing a range of physicochemical properties. Structural, morphological, thermal and electrical properties of *ortho*– and *meta*–substituted polyanilines have been widely reported [1,2,4,11]. However, systematic reports on poly(*p*-anisidine) (PPA) have not been found in scientific literature. There is a significant lack of information on pure PPA [19]. However, some reports have been devoted to develop PPA-based nanocomposites [17,18,20,21].

The preparation of electroactive nanocomposites based on PPA and clay were performed by oxidative polymerization [21], and the intercalation of PPA was confirmed by the increased interlayer spacing and exfoliation forms. The synthesis of PPA/TiC and PPA-co-

ANI/TiC nanocomposites was also reported [18]. The authors explored the use of PPA as an alternative to polyaniline in anodic materials for hydrometallurgy. Nanocomposites were also successfully synthesized by oxidative polymerization of *p*-anisidine and/or aniline monomers on TiO_2 nanoparticles [20], producing electroactive microspheres. The authors proposed their use as fillers for antistatic and anticorrosion coating. Nanocomposites based on PPA and ZnO were synthesized by adding the semiconductor metal oxide to the polymeric solution [17]. The electrochemical conductivity evaluation suggested blends with enhanced conductivity nature.

In order to evaluate the structural, morphological, spectroscopic and electrical properties of PPA, conventional oxidative polymerization of *p*-anisidine was carried out. The effect of the concentration of monomer, ammonium persulfate (APS) and HCl on the percentages of crystallinity of each PPA sample was considered. X-Ray diffraction technique (XRD) was applied in order to examine the long-range order achieved as a consequence of very short-range interactions, and also to estimate the percentage of crystallinity. The ^{13}C NMR experiments were useful to confirm the head-to-tail and head-to-head mechanisms of polymerization of PPA. Scanning Electron Microscopy (SEM) was useful to correlate the influence of the mechanisms of polymerization on the polymer morphology: a detailed and local description of complex scaling behaviors from the SEM images were obtained using multifractal analysis. Fourier-transform Infrared Spectroscopy (FTIR) was applied for molecular structural characterization, as well as to confirm the mechanisms of polymerization of PPA. Density Functional Theory (DFT) [22–24] was employed to investigate the molecular geometry optimization of PPA through the results obtained experimentally by ^{13}C NMR. Theoretical FTIR spectra were computed using time-dependent DFT [25] to access molecular structure and electronic configuration. These results were correlated to those obtained experimentally. Finally, the electrical conductivity of the developed polymers was accessed by Complex Impedance Spectroscopy analysis.

2. Brief Considerations on Polyaniline and Its Derivatives

The development of Intrinsically Conducting Polymers (ICP) – also known as conjugated polymers – with reversible oxidation/reduction behavior has allowed novel perspectives on the physicochemical evaluation of macromolecular compounds and technological applications [1–3]. Polyaniline (PANI) is the oldest and the most common representative of conjugated polymers [4] mainly due to its redox and acid–base properties, high thermal stability, and controlled electrical conductivity [5]. However, the rigidity of the polymer chain and, consequently, its difficulty to melt and insolubility in most organic solvents limit its potential application in modern technologies [3].

Several reports on the synthesis of PANI derivatives have been conducted to increase solubility and maintain electrical properties at acceptable levels. The introduction of long functional and flexible polar functional and alkyl groups linked mainly to the polymer backbone represents an alternative to obtain soluble polymers in a larger variety of organic solvents [6]. As a result, different crystal structures, percentage of crystallinity, morphologies, range of electrical conductivity and polymerization mechanisms have been proposed due to the wide methodology reported to developed PANI derivatives [7,8].

The incorporation of side groups at the *ortho*–, *meta*– or *para*–positions into the polymer backbone represents a common technique to improve solubility. Recent studies on substituted polyanilines show the importance of investigating the influence of substituent groups on polymer properties [7,9]. Electron–donating side groups cause distortion in the polymer backbone, reducing conjugation and improving flexibility. When compared to the pure conducting PANI, the derivatives usually present reduced electrical conductivity. However, the conducting range can also be controlled and depends on several parameters such as the nature and size of counterions/doping acid and time of polymerization [7,9,10].

The ring-substituted derivatives of PANI, such as poly(*o*-methoxyaniline) (POMA) [9,11], poly(*o*-ethoxyaniline) (POEA) [12,13], poly(*m*-anisidine) (PMA) [7] and poly(*p*-anisidine) (PPA) [14], have been constantly studied due to their improved solubility, electrical and optical properties, low cost, easy processability, environmental stability and relatively simple preparation. Some studies have been devoted to produce PANI derivatives without significantly compromising their electrical properties when using alkyl and alkoxy substituents in the ring, such as $-OCH_3$ (*o*–methoxy) and $-OCH_2CH_3$ (*o*–ethoxy). The preparation of derivatives involves similar methodology than that of aniline polymerization [15,16].

The crystal structure, morphology, thermal stability and conduction mechanisms have also been proposed for the prepared derivatives. However, the evaluation of different aniline derivatives are very far from completion and this field often looks fragmented [1]. Only POMA and POEA have been intensively investigated [11,13,17,18], while there is a lack of information on *meta* [7] and *para*–anisidines [14]. As a result, the connections between the conditions of synthesis and physicochemical properties represents an important area of research.

The properties of PANI and its derivatives are determined by the regular structure of their molecular chains. The polymerization of aniline is a chain process: the monomer units are successively appended to a polymer chain bearing an active terminal group. The polymer backbone is usually composed by *para*-substituted monomeric units in a head-to-tail polymerization. However, as will be shown in this present work, there may be a combination of head-to-tail and head-to-head polymerization in the case of poly(*p*-anisidine). Chain propagation involves repeated activation–deactivation mechanisms, which imply oxidation–reduction. Inactive polymer chain is activated by the action of oxidant, but the subsequent reaction with monomer leads to reversible reduction and deactivation. During the reduction process, polymer chain extends due to addition of monomeric unit [5].

The regularity of molecular structure determines polyconjugation and distinguished properties, which are intrinsic to the polymer and allow specific applications. Modern

applications on PANI and its derivatives are mainly focused on nanoadsorbents [19], electro-responsive smart suspension [20], electrorheological and magnetorheological applications [21], flexible supercapacitors [22], membranes for ultrafast nanofiltration [23], organic solar cells [24], tissue engineering [25] etc.

2.1. Ring-substituted Derivatives of PANI

Despite the prominence that PANI presents within the class of ICP, there are some to its use on a large industrial scale, such as low solubility in organic solvents, low mechanical flexibility and processing. Several alternatives are still proposed to overcome these limitations. The introduction of alkyl– and aryl–linked substituents in the polymer chain is a common alternative to synthesize soluble PANI in organic solvents or aqueous solution [7,8,10,12].

Emeraldine-salt form of PANI (ES-PANI – the conducting form) is insoluble in most organic solvents and is also infusible. The insolubility of ES-PANI can be attributed to the rigidity of its main chain, resulting from the existence of a strongly conjugated π–electron system. Electron–donating substituent groups at positions 2 and 5 of the ring cause distortions in the main chain, reducing conjugation and increasing flexibility. As a consequence, there is an increase in solubility and a decrease in electrical conductivity [16]. Recent studies with substituted polyanilines show the importance of investigating the influence of substituent groups on polymer properties [26].

Some studies have been developed to produce PANI derivatives without, however, compromising considerably its electrical and electrochemical properties, showing that PANI processability is improved when alkyl– and alkoxy– substituents such as $–CH_3$, $–OCH_3$, $–SO_3H$ and $–OCH_2CH_3$ are inserted in the molecular structure. The preparation of PANI derivatives involves the same methods used for the polymerization of aniline [15,16]. Among the PANI

derivatives, poly(*o*-methoxyaniline) (POMA) and poly(*o*-ethoxyaniline) (POEA) are the most representatives on scientific reports.

Considerable efforts have been devoted to correlate synthesis conditions with structural and electrical properties of chemically synthesized conjugated polymers. The doping process is dependent on the nature of the dopant acid [7,8], and conformational modifications of these polymers are influenced by the substituents electron donating groups present along the aromatic rings [27]. For this reason, the functionalized side groups at the *ortho*–, *meta*– or *para*–positions in PANI derivatives have allowed a range of physicochemical properties [28].

Structural, morphological, thermal and electrical properties of *ortho*–substituted polyanilines have been widely discussed [10,11,29]. However, there is a reduced number of studies reporting poly(*m*-anisidine) – PMA and poly(*p*-anisidine) – PPA. For this reason, systematic investigations of their structural, morphological and electrical properties are of considerable importance. [30–33]. Studies on the *ortho*–substituted polyanilines have been constant objects of interesting reported works [34–37]. Among the polyanisidines, POMA and POEA are the polymers most commonly reported in the scientific literature because of their higher electrical conductivity values when compared to PMA and PPA, in addition to their easier polymerization due to the lower oxidation potential [32].

The oxidative polymerization of nanostructured PANI and polyanisidines was performed using dodecylbenzene sulfonic acid, ammonium persulfate and phenylamine to obtain a star-based polymer morphology. The results confirmed the solubility, in addition to the increase of electrical conductivity, reduction of viscosity and density when compared to homopolymers obtained from the same monomers [38,39].

Reports have also focused on the reactivity of *o*-anisidine, *m*–anisidine and *p*–anisidine monomers with metallic cobalt. The difference in affinity was verified as a function of the region of the adsorptive surface sites and the position of the $-OCH_3$ groups. For the *ortho*–positioning, as it is closer to the amine group, the tendency of interaction with the surface was vertical, while

for *meta*– and *para*–positions, the approach was of the flat surface type. It was also found that the *meta* isomer has a higher affinity for protons, while the *ortho* isomer has a higher oxidizing characteristic [31,40].

2.1.1. Poly(*o*-methoxyaniline) – POMA and Poly(*o*-ethoxyaniline) – POEA

POMA is derived from PANI and its structural difference is based on the methoxy group (–OCH_3) located at the *ortho*–position of the carbon rings. Despite this difference, POMA has physical properties quite similar to those of PANI. However, the solubility of POMA is higher mainly due to the effects promoted by the presence of the methoxy group: induced torsion in the polymeric chain and increase of polarity with modification of the planarity effect. **Fig. 1** shows the POMA tetramer in basic and salt forms [8].

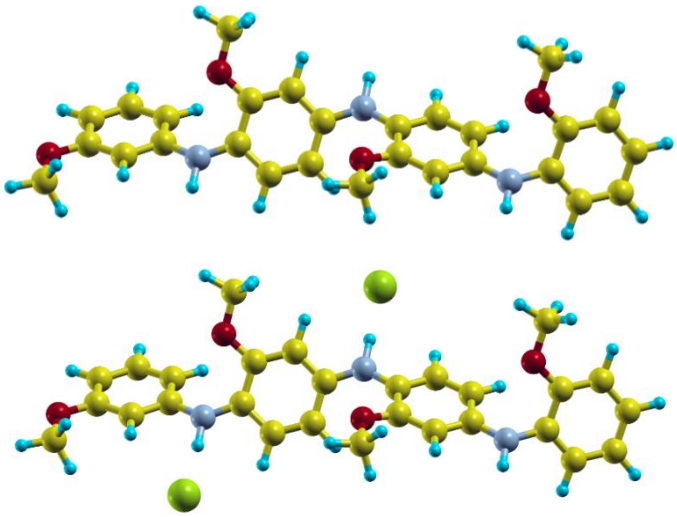

Figure 1. Molecular structure of a POMA tetramer as (a) Emeraldine-base (EB–POMA) and (b) Emeraldine-salt (ES–POMA) forms.

Similarly to PANI, POMA can be obtained in different oxidation states: leucoemeraldine, emeraldine and pernigraniline, and the emeraldine oxidation state can be found in basic (non-

electrical conductive) or saline (electrical conductive) forms. The conversion of base to emeraldine-salt form can be achieved via protonation in acidic medium [41].

POMA has been widely studied in the form of powder obtained by chemical synthesis or in the form of films obtained by electrochemical synthesis. The preparation of POMA by oxidizing the monomer with $(NH_4)_2S_2O_8$ and doping using HCl resulted in a soluble polymer in DMF, acetic acid and sulfuric acid [16].

Chloride Salt of ES-POMA was prepared by oxidative polymerization in the presence of hydrochloric acid (HCl) elsewhere [11]. A detailed systematic observation of crystalline phases of the doped form was proposed, differing in their semi-crystalline structures and morphology. The authors revealed that the crystallinity increased very slowly because of the steric hindrances due to the greatest volume of the *o*-methoxy group. XRD analysis showed different patterns as a function of the time of polymerization. The Le Bail refinement allowed the determination of the unit cell parameters, changing the ‘‘a’’ and ‘‘b’’ values (when compared to the undoped PANI tetramer) in order to accommodate the *o*-methoxy groups and counter ions. The SEM analysis showed that the increasing of the time of synthesis resulted in the reduction of the globular vesicular structure together with increased crystallinity. The electrical conductivity increased from 5.18×10^{-7} to 8.89×10^{-7} S/cm when the time of synthesis was increased.

Doped POMA polymers were recently reported and obtained using different dopant acids [8]. The structural, morphological, thermal and electrical properties of the synthesized polymers were significantly related to the nature of the dopant acid. The doping acid influenced on the polymer crystallinity, and angular displacements of diffraction peaks were associated to changes in lattice parameters. The polymer crystallites seemed to reach a maximum average size, independently of the percentage of crystallinity or the nature of the counter ion. Each synthesized polymer presented specific morphology, which was considerably related to the nature and concentration of the dopant acids. Moreover, well defined morphology was not

related to high percentage of crystallinity. The most thermally stable polymer was obtained using H_3PO_4 as doping acid. The electrical conductivity of POMA was found to be considerably dependent on the counter ion size: the polymer POMA/HCl presented the highest conductivity value among all the evaluated polymers probably due to its smaller counter ion size, as well as an efficient doping process.

2.1.2. Poly(*m*-anisidine) – PMA

Few works have focused on the poly(*m*-anisidine) (PMA) providing information on its characteristics and properties through diversified characterization techniques. A recent paper evaluated experimentally and theoretically by DFT the effect of the use of different acids in the chemical synthesis of PMA [7]. Structural, morphological, thermal and electrical properties of the prepared PMA polymers were significantly related to the nature of the dopant acid, as also observed in the case of POMA. **Fig. 2** shows the molecular structures of the doped forms of PMA as a function of the doping acid.

The authors revealed that the lattice parameters were significantly related to the counter ion sizes mainly along [010]. A spherical-like form of crystallites was found in the PMA doped with H_2SO_4. However, the doped PMA presenting smaller counterions (HCl or HNO_3) presented prolate-like crystallite shape. All polymers were constituted of solid spheres, and larger counter ion size resulted in smaller microparticles. The theoretical calculation revealed a charge transfer between polymer chains and counter ions. The polymer PMA/HCl presented the HOMO band partially filled due to the new energy states generated by the counterions Cl. The polymer PMA/HNO_3 presented new energy bands created by acid doping; however, the molecular counter ion NO_3 has higher electron density and the mainly contribution was due to the oxygen atoms. In this case, the charge transfer was verified along the whole network formed by the interaction of the molecular counter ion NO_3 and the polymer chain. The HOMO band of

the polymer PMA/H_2SO_4 was verified to be fully occupied, resulting in a near-zero gap semiconductor behavior. As shown by the load distribution visualization map of the doped polymers, the highest charge density was located around the nitrogen and oxygen atoms, contributing to the conducting properties [7].

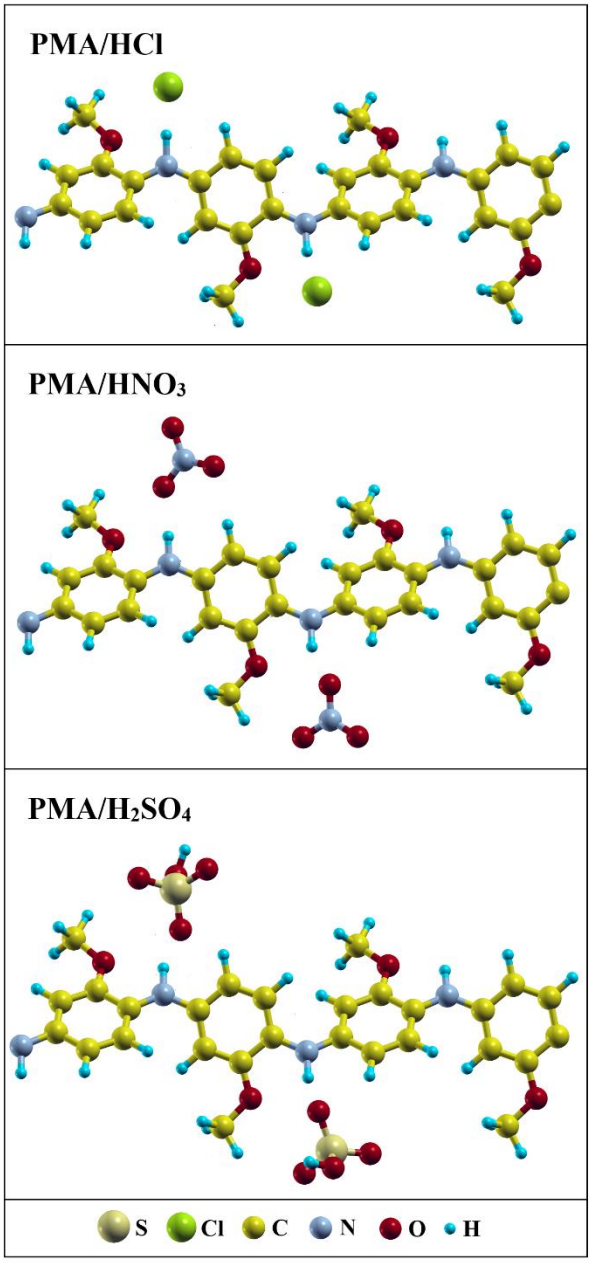

Figure 2. Geometric optimization of the doped PMA doped with HCl, HNO_3 and H_2SO_4 [7].

The synthesis of PANI and its derivatives through the chemical oxidation of corresponding monomers in the presence and absence of CSA was proposed elsewhere [42]. The authors revealed that the oxidation of aniline in both cases produced nanotubes, while the

oxidation of aniline derivatives does not produced such one-dimensional nanostructures under the same experimental conditions. For aniline derivatives, the chemical oxidation in the presence of camphor sulfonic acid (CSA) mainly produced hollow microspheres. The role of CSA was mainly to stabilize the droplets of aniline derivatives during oxidation, resulting in the formation of the well-defined hollow microspheres. In the absence of CSA, the main factors to define the polymer morphology were stability of droplets and the rate of exothermal reaction. The fast exothermal reaction influenced on the formation of microspheres.

2.1.3. Poly(*p*-anisidine) – PPA

The *p*-anisidine is the most toxic among the anisidine monomers, causing damages to the blood when ingested orally, by inhalation or skin contact [43]. This monomer has the methoxy group in the *para*–position related to the aromatic amine. Several studies have focused on the chemical evaluation of the monomer. However, few reports have been devoted to investigate systematically the polymerization process, as well as the effects and applications of PPA in the development of novel composites. Among these reported studies, the electrical conductivity of PPA-based nanocomposites combined with ZnO was reported [14]. Another clay-based PPA composite was prepared and their optical and electrochemical properties were accessed [44]. Some authors investigated the physicochemical and spectroscopic characteristics of *p*-anisidine monomer treated with biofield energy [45], as well as the development of a chemically modified carbon paste electrode. The synthesis and properties of polyanisidines through differences in oxidative potential were also reported: changes were attributed to the redistribution of the electron density in the electroactive groups [1]. Finally, PPA-based TiC nanocomposites were prepared from the oxidative polymerization of *p*–anisidine and/or aniline with TiC nanoparticles for application in anodic coatings for hydrometallurgical purposes [46].

The most important topic on the PPA research is focused herein on the understanding of the polymerization mechanism. No reports have been found proposing a consistent mechanism. Furthermore, the PPA morphology and crystal structure is also certainly the proposal of the present research.

2.2. Morphological and Crystal Structure of PANI and its Derivatives

Although PANI has already been extensively studied, its structural and morphological aspects remains an interesting research topic, and novel and interesting information have always been accessed. Considerable efforts have been dedicated on the development of novel synthesis methodologies on nanostructured forms of PANI and its derivatives allowing novel applications [47].

Several organic materials are known for their ability to form different morphologies in a wide range of sizes. However, few conjugated polymers have revealed as many different morphologies at nano and micro scales as those found from the chemical oxidation of aniline. The nanostructured morphologies of PANI present an impressive diversity [48].

The conventional polymerization of aniline usually results in granular and nanofibers morphologies. However, the nanofibers growth started from a nucleus and depend on the head–to–tail coupling between the aniline radicals. The conventional and interfacial methodologies allowed the crystallization of PANI in a range of crystal structures and lattice parameters. Recently, the coexistence of four different types of morphologies (nanoplates, nanorods, nanofibers and nanoflowers) were identified in the PANI synthesized by interfacial polymerization [48]. These main architectural elements might be useful for more complex geometric structures [5]. **Fig. 3** shows the SEM images of PANI, as well as their *ortho* (POMA), *meta* (PMA) and *para*–methoxy (PPA) derivatives highlighting their specific morphologies formed by conventional chemical oxidative polymerization.

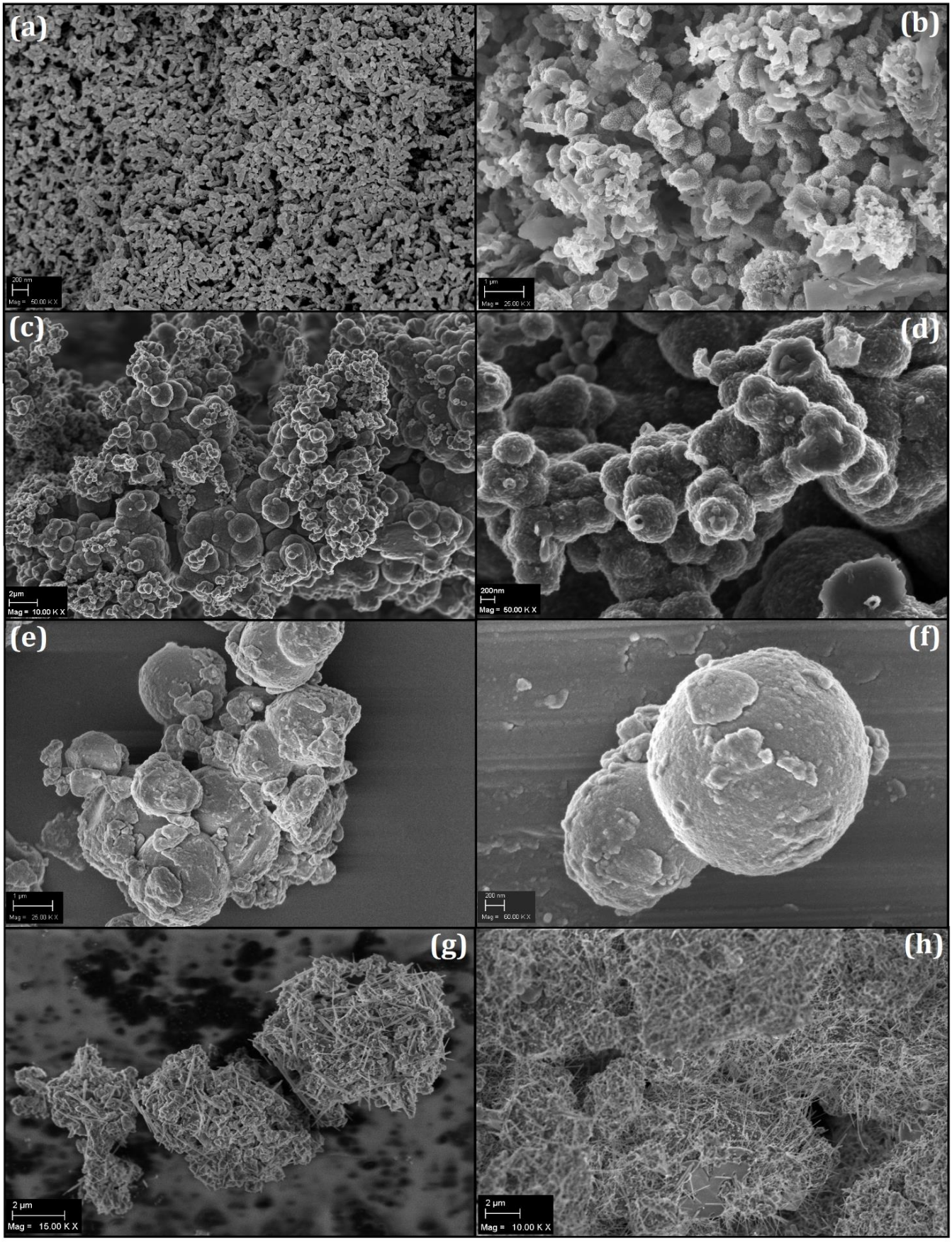

Figure 3. (a-b) PANI [48], (c-d) POMA [10], (e-f) PMA [7] and (g-h) PPA synthesized using ammonium persulfate and HCl 1M.

Understanding the structure, morphology and property relationship is of particular importance, since many physicochemical properties of materials can be modified by adjusting their size or morphology. The manipulation of structure and morphology of conjugated polymers has grown considerably [49–51] due to the potential advantages of obtaining semiconducting materials at nanoscale.

Some solid-state reactions result in the formation of polymer crystals. The final morphology is a guideline about the polymerization mechanism. A crystal can be defined as the solid state portion of matter in which long-range atomic order is observed in 3D space, inducing anisotropic properties in this portion of matter. This atomic organization is infinite in the ideal crystal, while in real crystals it extends to a scale considered appropriate for the description of its properties. Polymeric molecules can also form ordered arrangements, presenting structural regularity in different levels of spatial orientation and, consequently, of crystallinity. Therefore, the polymeric crystallinity is a consequence of the molecular packing [52].

Polymer crystallization occurs less easily when compared to other types of materials due to the complexity of polymeric macromolecules. However, depending on the chemical nature as well as some synthesis conditions, a mass percentage of the polymers can crystallize. The percentage of crystallinity of semi-crystalline polymers can range from completely non-crystalline to approximately 95% crystallinity. The application of stress in polymer processing can influence the crystallinity because the deformation processes might result in chain alignment. Furthermore, for some polymers, the percentage of crystallinity is related to the cooling rates during solidification.

In the case of conjugated polymers, several synthesis parameters can influence on the percentage of crystallinity, such as the nature and concentration of the dopant acid, polymerization time and temperature, reagent addition rate etc [4,9,53]. The percentage of crystallinity influences some physical, mechanical and optical properties of polymeric

materials, in addition to the electrical conductivity. **Fig. 4** shows the XRD patterns of PANI, POMA, PMA and PPA, and their correlated morphology obtained from the SEM technique.

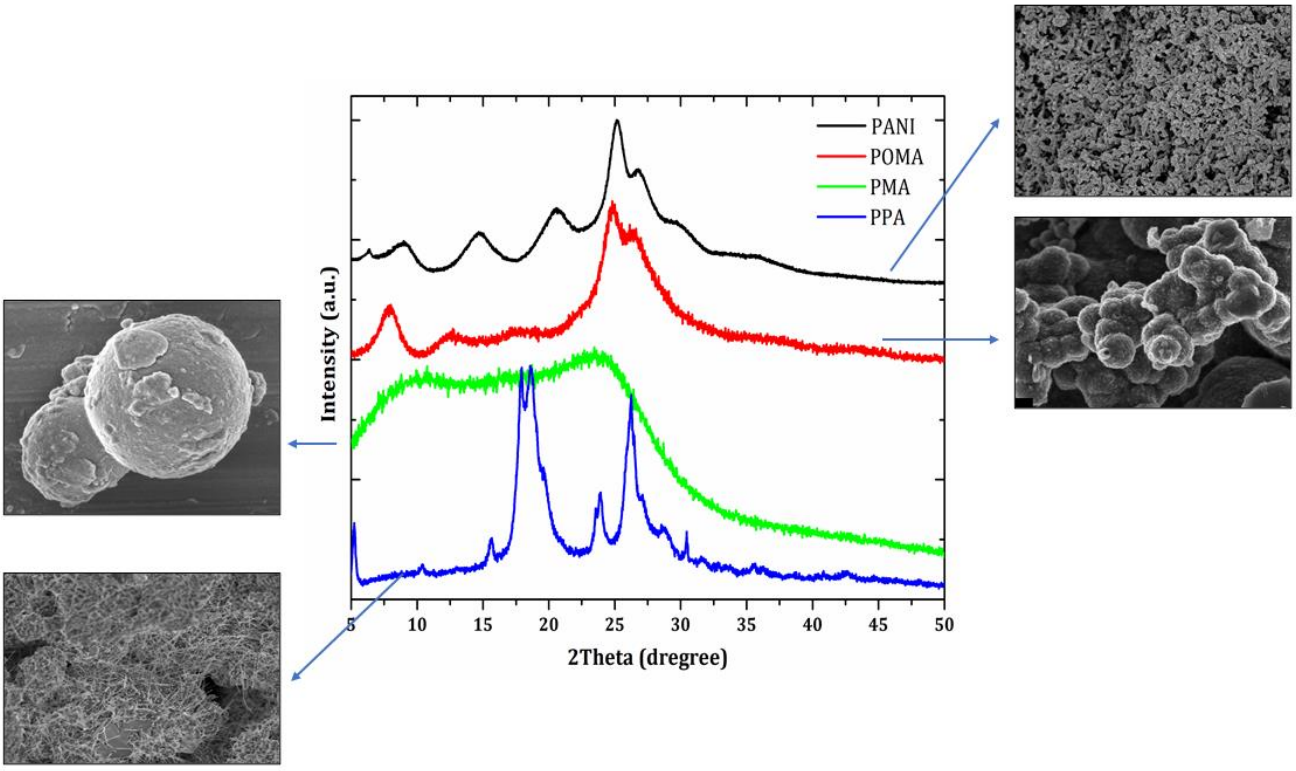

Figure 4. XRD patterns of PANI [48], POMA [10], PMA [7] and PPA, and their correlated morphology obtained from the SEM technique.

Several inorganic materials have well-defined and thermodynamically/kinetically stable crystal structures, which can be used to control their nanostructures. Considering PANI and its derivatives, alkoxy substituents in the ring (such as the methoxy group) play an important role on the polymerization and molecular packing, influencing on crystal structure and morphology (as shown in **Fig. 4**). Such crystals are very useful as models to understand the crystallization behaviour of long chain molecules [52]. However, many organic materials (especially conjugated polymers) do not have an unique crystalline structure and/or morphology for an specific polymer, being dependent on the synthesis methods and reagents [10,48,54]. This is particularly true for PANI, and several nanostructures have been observed according to different methods of synthesis [55].

Possible molecular models of the chain growth are developed on the basis of the morphological observation. In general, PANI exhibits low to medium range of crystallinity; however, several studies also revealed highly percentage of crystallinity [55]. Solid-state polymerization is considered as a phase transitions from the crystalline phase of the monomer to the phase of the growing polymer. The XRD patterns of PANI and its derivatives present diffraction peaks below $2\theta = 30°$ [10,48,54], which are attributed to the parallel and perpendicular periodicity of the polymer chain. The polymer chains grow as isolated macromolecules within the monomer lattice. A quantitative conversion can be reached in some cases without phase separation, comprising a method to produce macroscopic, extended chain polymer crystallites [52].

The triclinic crystal structure of PANI and POMA were reported, and the unit cell parameters are influenced by the nature of the counter ions in the case of doped forms. In this case, the unit cell volume is increased due to the incorporation of counter ions into the polymer molecular structure as a result of electrostatic interactions [10,48,56]. The influence of the nature of counter ions on the unit cell parameters were evaluated by Le Bail structural refinement and influences directly on the [010] direction [10,56]. However, the crystal structure of PANI was also reported as monoclinic [57] .

The opposite type of solid-state polymerization is the polymerization in non-crystalline zones. Here, the reaction starts preferentially at dislocations, defects, or at the boundaries of the monomer crystal, where a polymer phase is formed [52]. The reduction of crystallinity in PANI and its derivatives have been achieved by heat treatments or neutralization process [11,54,58]. In this case, the degradation of the polymer chains due to the effect of temperature, or the withdrawn of counter ions by chemical neutralizing action were reported. Thus, the knowledge of the crystal structure of the monomer as well as the molecular structure and morphology of the polymer as polymerized is necessary to propose the mechanism of a particular solid-state polymerization [52].

2.3. Molecular Structures of Polyanilines

The synthesis of PANI and its derivatives includes two interrelated processes, including the assembly of monomeric units resulting in the growth of macromolecules, and self-organization of the growing chains into supramolecular structures [59]. Most of these structures cannot be dissolved or melted without destroying the polymer chain, which would change the polymer properties. Therefore, the synthesis methodology represents the only tool to control the structure of the chains and obtain nanostructured forms of conjugated polymers or composites (when the polymer is synthesized in the presence of other materials).

PANI and its derivatives can be synthesized in a variety of oxidation states differing in their chemical and physical properties, as shown in **Fig. 3**.

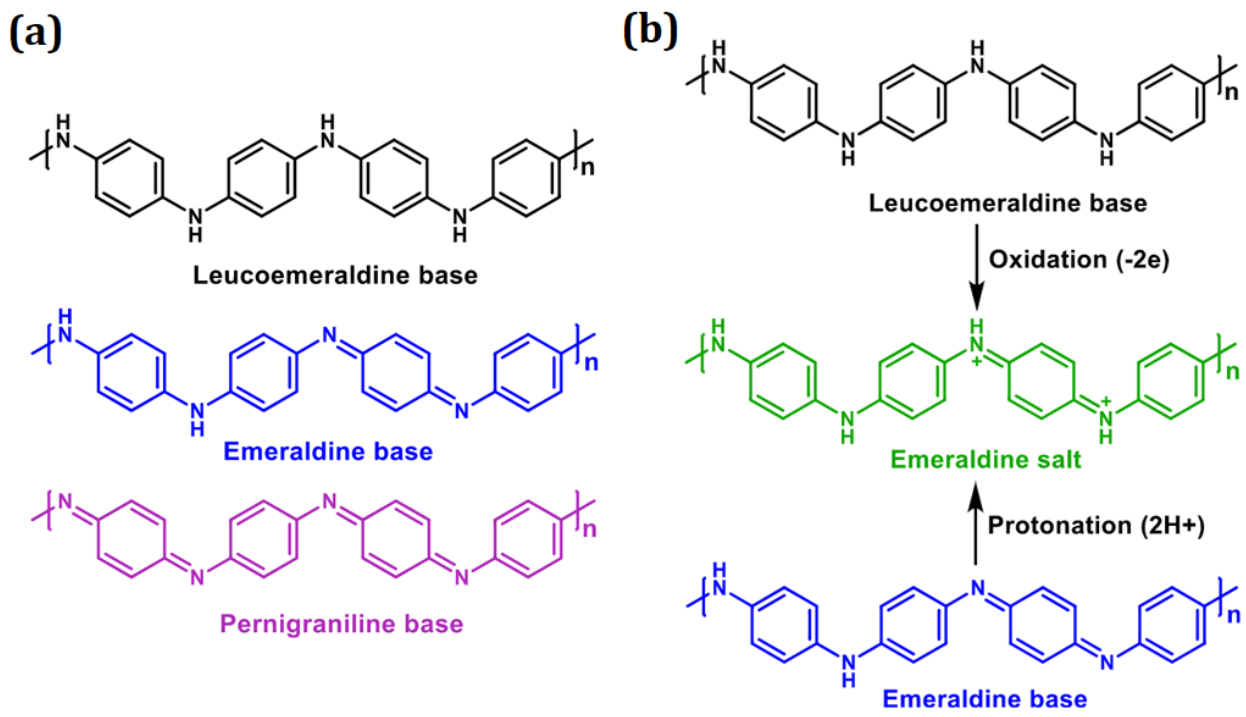

Figure 5. (a) Different forms of PANI and (b) Formation of an emeraldine-salt form of PANI by oxidation and protonation of bases.

MacDiarmid firstly proposed three different types of basic PANI in 1997 [60], including fully reduced leucoemeraldine (LEB–PANI), half-oxidized emeraldine-base form (EB–PANI),

and fully oxidized pernigraniline (PG–PANI) (**Fig. 5(a)**). Among them, EB–PANI can be converted into the conducting emeraldine-salt form (ES–PANI) by doping via protonic acid [**Fig. 5(b)**]. Different forms of PANI show different colors like LEB–PANI is white/clear and colorless, EB-PANI is blue in base form and green in ES-PANI form, and PG–PANI is blue/violet [61]. The most common form, ES–PANI, has electrical conductivity similar to the traditional inorganic semiconductors (up to 100 S/cm, greater than common polymers (< 10^{-9} S/cm), but less than typical metals (> 10^{4} S/cm)), and can be converted to the non-conducting form, EB–PANI, when treated with a base such as ammonium (NH_4OH) or sodium hydroxide (NaOH) [59].

Similar oxidative properties can be reached in the PANI derivatives, such as POMA, PMA and PPA [7,10,11]. Despite being known for over 150 years, research on PANI and its derivatives has been focused mainly on understanding the chemical structure and electronic conduction mechanisms, developing polymerization techniques and chemical and physical modification methods to improve their processability, crystallinity and electrical conductivity.

While in many other conjugated polymers the conductivity is a function of the oxidation state (the number of π–electrons added to or removed from the neutral polymer backbone), PANI was the first case where the conductivity depends *(i)* on the oxidation state of the polymer and *(ii)* the degree of protonation of the nitrogen atoms in the molecular structure. Thus, the doping process of PANI is based on protonation, without changing the number of electrons associated with the polymer chains.

During the doping process, oxidation and/or reduction reactions occur and the counter ions (dopant) remains in the polymer matrix. The ES–PANI is the first successful example of doped polymer presenting highly electrical conductivity from a process in which the number of electrons remains unchanged (protonation). The protonation of EB-PANI using a protonic acid increased the electrical conductivity about 10 orders of magnitude, leading to the ES-PANI form. Deprotonation occurs reversibly by similar treatment with aqueous base solution [62].

This doping mechanism is significantly different from redox doping (oxidation or reduction), which involves partial addition (reduction) or removal (oxidation) of electrons from the polymer chain. The doping mechanism of PANI by protonic acids is shown in **Fig. 6**. First, the protonation reaction occurs on the imine N atoms. Then, phenylenediamine radical cation is formed by intramolecular change transfer. The charge of N atoms is delocalized to the neighboring benzene ring and N atoms by conjugation. Thus, the transmission of the π-electron is not limited between two C atoms, but in the whole system [62].

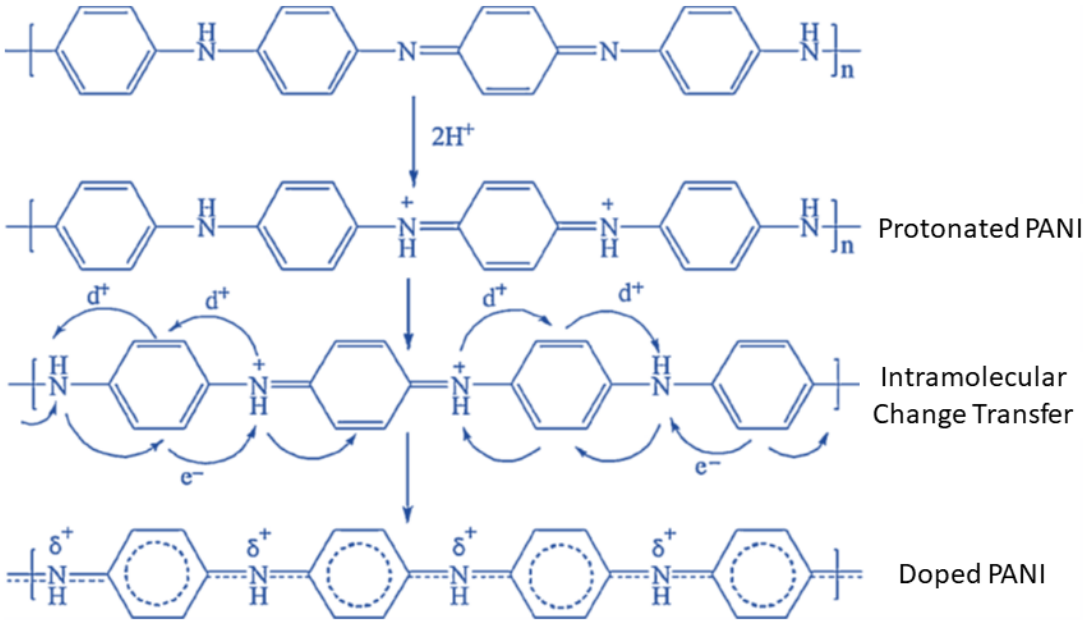

Figure 6. Doping mechanism of PANI by protonic acids.

As shown in **Fig. 6**, the protonation process occurs only in the imine segment of the polymer chain, consisting of a chemical reaction of the proton with N atoms in the imine segment, together with a diffusion of counter ions from the aqueous solution to the polymer. The emeraldine-salt form can be considered in terms of molecular structure as a partially protonated state, implying that the molecular structure of ES-PANI is determined by both the oxidation and the protonation state.

2.4. Conducting Mechanisms

PANI is among the most prominent representatives of electrically conductive polymers. It has a controlled electronic conductivity in the range of 10^{-10} to 10^{1} S/cm as well as ionic conductivity [59]. The basic requirement for an organic molecule to conduct electricity is the availability of alternate double bonds: conjugated double bonds is responsible for the delocalization of π–electrons in organic molecules. Increase in delocalization of π–electrons results in the decrease of the *gap* energy between Highest Occupied Molecular Orbital (HOMO) and Lowest Unoccupied Molecular Orbital (LUMO) [63].

For an infinite polymer chain, the coulombian interactions between the π-orbitals results in the delocalization of the electrons along the polymer chain. As a result, an approximately continuous distribution of energy states occurs, creating a distribution of energy bands. The interaction between the π–ligand orbitals (HOMO) resembles the Valence Band (VB) and the interaction between the π^*–antiligand orbitals (LUMO) resembles the Conduction Band (CB), and the difference of energy (HOMO - LUMO) is denoted as E_g, as shown in **Fig. 7** [64].

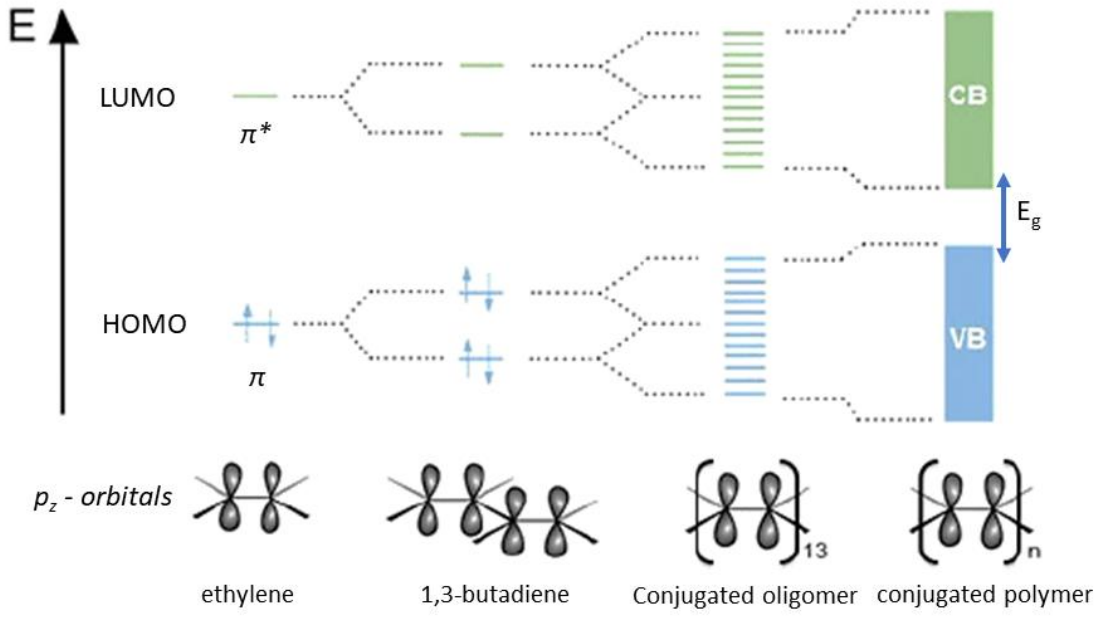

Figure 7. HOMO and LUMO bands of conjugated organic molecules.

The energy difference between HOMO and LUMO represents the E_g value of conjugated polymers. Depending on the electronic occupancy and the E_g value, a solid material is classified as insulator, semiconductor, or conductor. Thus, almost all conjugated polymers are classified as semiconductors, presenting E_g values in the range from 1.5 to 3.2 eV. For comparison, the E_g values of saturated insulating polymers are greater than 10 eV, which restricts the promotion of electrons from VB to CB band in order to promote electrical conductivity [65].

In conjugated polymers, the doping process represents the mechanism by which the polymer is exposed to oxidizing or reducing agents to effectively convert conjugated polymers to conductive polymers. Doping of conjugated polymers is reversible and therefore the polymer chain is not permanently altered after this process. Due to the doping process, charge centers are generated within the conjugated polymer and the counter ions are associated with this charge center in the polymer matrix to maintain electroneutrality.

The conduction process in doped polymers results in the generation and disappearance of charged sites in the conjugated polymer chains, and the electroneutrality of the doped polymer is maintained by incorporation and repulsion of mobile counterions [66]. In their doped, electrically conductive forms, conjugated polymers typically present positive charges (polarons or bipolarons) along their polymer chains, which are balanced by the incorporation of counter ions. These anions may consist of a variety of chemical groups, such as Cl^-, HSO_4^-, ClO_4^-, NO_3^- [67], even larger species such as (CSA^-), and biopolymers [41,65,68].

The oxidation of the conjugated polymer generates a cation radical, or polaron hole, while reduction produces an anion radical, or polaron electron. Polarons allow the appearance of new well-defined energy states within the bandgap [69]. A cation radical partially delocalized in a polymer segment is known as polaron, presenting spin ½. Both radical and cation are coupled to each other by a local resonance. The presence of a polaron induces the creation of a quinone sequence within the polymer chain. The lattice distortion produced is of greater energy than the remaining portion of the chain. The creation and separation of these defects cost

energy, which limits the number of quinoid rings that can bond to these two species together. Removal of a second electron results in the bipolaron formation, which is defined as a pair of equal charges (dication with zero spin), associated with strong distortion of the reticule. For conjugated polymers presenting high concentrations of dopants, bipolarons create energy bands symmetrically located above the valence band and below the conduction band. This results in a Fermi energy level close to the maximum (highest energy state) of the valence band, which is partially filled. This is a necessary condition for metal conduction [69].

Theoretical studies show that bipolaron is thermodynamically more stable than two separated polarons due to the coulombic repulsion of two charges confined at the same site and due to the decrease in ionization energy compared to the formation of two polarons. Thus, a bipolaron is a dication forming part of the polymeric structure, presenting positive charges located at a certain site. These charges can occur at many sites in the polymeric structure [70,71].

The conjugated system of a macromolecular compound determines the level of charge carrier mobility. The conductivity of PANI depends on the content and mobility of positive polarons (radical cations on nitrogen atoms, charge carriers) formed during oxidation. The PANI chains are regular sequences of monomeric units providing conjugation of the π–electron clouds on the aromatic ring and the unshared electron pair on the nitrogen atom, which overlap above and below the plane of the polymer chain (**Figure 4**) [59].

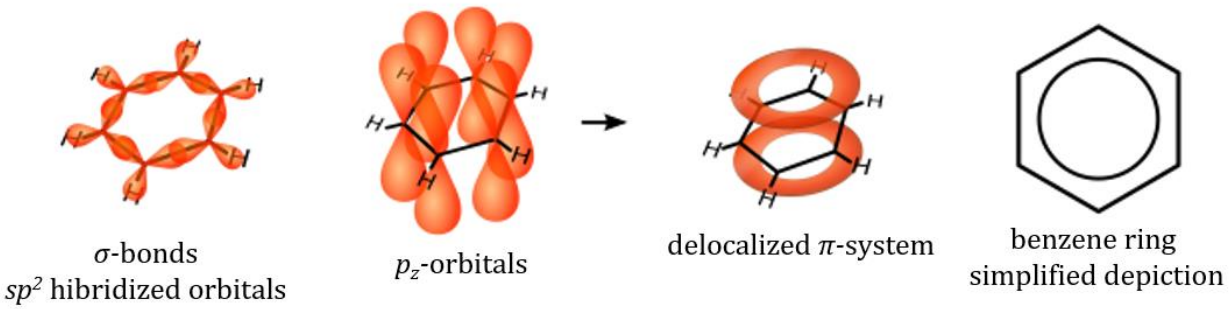

Figure 8. Delocalized model of benzene. Delocalized electrons from a ring of negative charge above and below the plane of the benzene ring.

The presence of both electron-donating and electron-withdrawing groups in the macromolecule results in a decrease in electrical conductivity, but it is caused by different reasons. An increase in the number of substituents at the aromatic ring leads to a larger torsion angle relative to monosubstituted derivatives, causing a decrease in electrical conductivity [72].

The presence of an oxygen-containing electron-donating group at the *ortho* position of aniline, like with alkyl groups, results in a decrease in electrical conductivity. However, despite the narrowing of the band gap in poly(*o*–methoxyaniline) (POMA), the conductivity of this material is significantly lower than that of alkyl derivatives which, in turn, widen the band gap. Apparently, this can be explained by the electronic effect of alkoxy groups on the properties of the polymer. The electrical conductivity of POMA is higher than that of its isomer, poly–2–aminobenzylalcohol. The larger volume of the $–CH_2OH$ group in comparison with $–OCH_3$ results in a more twisted polymer with a low degree of conjugation and low conductivity. Based on this information, it was assumed that an atom with a low van der Waals radius (e.g., oxygen) favors the formation of a polymer with good electrical properties [59,73].

Defects in this regular structure can appear during the copolymerization of aniline with other monomers or after the introduction of aniline monomers with another configuration (*ortho*– or *meta*–substituted), leading to a dramatic decrease in conductivity [7,8,10]. The mobility of charges in the polymer structure is dependent on the void spaces, number of charge carriers in the structure and temperature. This mobility of charge carriers and defects associated with the interaction of dopant counterions along the chain basically defines the electrical conductivity. However, this charge movement is not performed only along the chain (intrachain), since the polymers have non-crystalline, crystalline regions and boundaries between regions (grain contours, defects, etc.) structure that contributes to the dispersion of charge [74]. As the conduction of charges in conjugated polymers is a basically diffusive process, three possibilities of charge transport are defined in its structure: intrachain transport, intermolecular transport (hopping) and interparticle transport (percolation).

Some structural characteristics in conjugated polymers such as chain planarity, degree of crystallinity, chain folds and crosslinks define the predominant type of charge transport. Normally, intermolecular transport is predominant. A greater distribution of non-crystalline regions (defects, non-periodic segments) dispersed in phases with a greater degree of organization (defined by the crystallites) is observed. In these crystallites, due to greater periodicity, charges are concentrated to form conductive islands in which intermolecular transport is the main means of electrical conduction [13].

The study of conjugated polymers is still lacking a model that explains the transport of electrical charge. There are models that are limited to describing structures with low conductivity, making an analogy to the diffusivity theory used for semiconductor materials. It is known that the conductivity is defined from the product between the number of free charge carriers (n) and the electrical mobility, (μ) = σ = |e|$n\mu$, considering crystalline semiconductor materials and metals with a fully crystalline structure. In non-crystalline structures, there is a high number of charge carriers, which, unlike crystalline materials, find mainly in the hopping transport mechanism a way to circumvent the obstacles imposed by the low structural definition, making it difficult to count free carriers and the degree of electric mobility [75].

Conduction can be defined in a generic way by providing the conductivity with a Boltzmann transport function (**Eq. 6**), where σ_e is the conductivity value, considering that the charge carriers have the same energy value.

$$\sigma = \int \sigma_e \left(\frac{\partial f}{\partial E}\right) dE \qquad \textbf{Eq. 6}$$

The charge transport is described according to **Eq. 7** for most semiconductor polymeric materials composed of two essential parameters defining the predominant type of transport in the structure, which are the transport edge (E_T) [76–78]. E/K_B is the reduced energy of the charge carriers, being electrons or holes, and $\sigma_{Eo}(T)$ is the transport coefficient.

$$\sigma_E(E,T) = \sigma_{Eo}(T) \times \left(\frac{E-E_T}{K_B T}\right)^S \quad \textbf{Eq. 7}$$

The transport edge can be related to the transport energy of the charge carriers below which there is no contribution of electrons or holes to the conductivity in a finite temperature range. For example, in insulating and semiconductor materials there are no charge carriers with energy lower than the transport energy (E_T) and therefore the transport edge is the edge of the band itself. Carriers with energy below the transport band need thermal excitation to cross the transport edge and conduct electricity.

Conductivity in doped polymers is determined at microscopic (intra and interchain) and macroscopic (interparticle) levels [66]. Hopping is a charge transport mechanism that usually occurs in clustered materials with localized charge carriers. Generally, these regions containing localized charges are known as conductive islands and may also be associated with regions of high crystallinity, **Fig. 9**. Due to the lower rigidity of the polymeric structure, the charge carriers induce a polarization that favors the location of charge carriers. In organic materials, electronic transport occurs mainly through the hopping mechanism. Electrons and holes in a polymer chain jump from one chain to another to carry charges, in contrast to inorganic crystalline solids where band transport is dominant due to the presence of a periodic crystal structure and well-defined state densities [79].

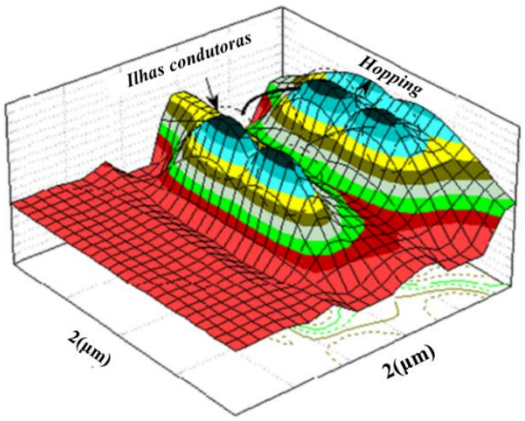

Figure 9. Map of forces obtained by Atomic Force Microscopy (AFM) showing conducting islands of poly(o-ethoxyaniline) film [80].

3. MATERIALS AND METHODS

3.1. Polymer Synthesis

Conventional oxidative polymerization of *p*-anisidine was carried out at 25 °C based on a Central Composite Rotational Design (CCRD) [81]. The number of treatments performed experimentally was composed of factorial, axial and central points (2^k + 2xk + central points), where *k* represents the number of parameters [*(i)* (*p*-anisidine) (g), *(ii)* ammonium persulfate (APS) (g) and *(iii)* HCl (*M*)]. **Table 1** shows the syntheses parameters.

Table 1. Syntheses parameters based on DCCR.

PPA	*p*-anisidine (g)	APS (g)	HCl (*M*)
PPA1	2	4	1
PPA2	2	8	2
PPA3	7	4	2
PPA4	7	8	1
PPA5	4.5	6	1
PPA6	2	4	2
PPA7	2	8	1
PPA8	7	4	1
PPA9	7	8	2
PPA10	4.5	6	1.5
PPA11	0.316700	6	1.5
PPA12	8.683380	6	1.5
PPA13	4.5	2.653360	1.5
PPA14	4.5	9.346640	1.5
PPA15	4.5	6	0.663340
PPA16	4.5	6	2.336660
PPA17	4.5	6	1.5

Solution I was prepared by solubilizing the *p*-anisidine monomer (2 g) in HCl 1*M* (150 mL). Solution II, on the other hand, was obtained by adding APS (4 g) in HCl 1*M* (200 mL). Solution II was added drop-by-drop to solution I. The resulting solution was maintained under constant stirring for 3 h. Then, the dark powder was vacuum filtered, washed with distilled water and maintained in a desiccator until reach constant weight to obtain the polymer labeled

as PPA1. The same methodology was performed using the parameters from **Table 1** to obtain PPA from PPA2 to PPA17.

3.2. XRD Analysis and Percentage of Crystallinity

XRD data were obtained on a Panalytical Empyrean diffractometer operating with CuK_{α} radiation at 40 kV and 40 mA. Data collection was performed in the angular range of $2\theta = 3° – 100°$, with a step size of 0.01° and 5 s/step. The simple area separation method [12,82] was applied to estimate the percentage of crystallinity. This method requires the separation/quantification of the integrated intensities from the crystalline and non-crystalline phases. A non-crystalline XRD pattern of PPA was obtained after the heat treatment of PPA1 at 300 °C for 30 min. Then, the ratio between the peak areas to the non-crystalline broad hallo was obtained using a routine software. The integration process was performed using the full XRD pattern from PPA1 to PPA17.

3.3. SEM Analysis

Powdered polymers were placed on a carbon tape. SEM imagens were taken at 25 °C on a microscope Carl Zeiss Supra 35 using 2.0 kV.

3.3.1. Multifractal Analysis

Fractals are geometric objects that, when moving away or approaching, the fractal set will always have a similar appearance, that is, it is said to be self-similar. In this case, the geometry used is no longer Euclidean, but fractal geometry. In this way, its topological dimensions are not non-integer values. To specify the complexity of a fractal object we use the

fractal dimension which measures the topographical variations in relation to the scale factor. The number of square cells, *N(ε)*, in relation to the scale factor *ε*, is expressed as

$$N(\varepsilon) \propto \varepsilon^{-D} \quad \textbf{(1)}$$

where *D* is the fractal dimension. So, in order to describe the size distribution of various objects, we make use of a scale (or power) law given by the equation

$$D = \lim_{\varepsilon \to 0} \frac{\log N(\varepsilon)}{\log \varepsilon} \quad \textbf{(2)}$$

which uses the box counting method. This method is widely used to find the fractal dimension of an irregular object. The objective of this method is to cover a fractal set with boxes of different sizes and to interpret how the number of boxes changes with respect to size.

However, fractal models are not able to clearly characterize the spatial anisotropy. On the other hand, a multifractal analysis can provides more information than a monofractal one. In this way, a detailed local description of complex scaling behaviors of SEM images was obtained using multifractal analysis based on a spectrum of singularity exponents. Data were extracted by computational routines [83–85] using the software MATLAB version 8.2.0.29 (R2013b). A multifractal system is composed of interconnected subsets with different fractal dimensions. Due to its simplicity and wide use, in this work we use the method of moments. Through the probability density in the i-th square, mass deposition at the local level can be estimated by eq. (3).

$$P_i(\varepsilon) = \frac{N_i(\varepsilon)}{\sum N_j(\varepsilon)} \quad \textbf{(3)}$$

where $N_i(\varepsilon)$ is the number of pixels containing mass in the i-th box of size ε and the denominator is the total mass of the system.

This system can be characterized when its surface contains *N(ε)* square cells, whose statistical sum is [86,87]:

$$Z(q, \varepsilon) = \sum_{i=1}^{N(\varepsilon)} P_i^q(\varepsilon) \sim \varepsilon^{\tau(q)} \quad \textbf{(4)}$$

where q represents the order moment with real values from −∞ (less dense areas) to +∞ (dense areas).

Many methods for the calculation of multifractal spectra have been used and in this work, we present two of them: the direct method and the indirect method (which uses the Legendre transformation). According to Chhabra, to calculate the multifractal spectrum by the direct method $f(\alpha(q))$ and $\alpha(q)$ can be obtained with the following equations:

$$\alpha(q) = \lim_{\varepsilon \to 0} \frac{\sum_{i=1}^{N(\varepsilon)} \mu_i(q,\varepsilon)\, log P_i^q(\varepsilon)}{\log \varepsilon} \quad \textbf{(5)}$$

$$f(\alpha(q)) = \lim_{\varepsilon \to 0} \frac{\sum_{i=1}^{N(\varepsilon)} \mu_i(q,\varepsilon) \log \mu_i(q,\varepsilon)}{\log \varepsilon} \quad \textbf{(6)}$$

where the parameter $\mu_i(q,\varepsilon)$ is:

$$\mu_i(q,\varepsilon) = \frac{P_i^q(\varepsilon)}{\sum_{i=1}^{N(\varepsilon)} P_i^q(\varepsilon)} \quad \textbf{(7)}$$

On the other hand, in the indirect method, to determine the multifractal characteristic the relationship between the generalized fractal dimension Dq and the exponent q is used. The generalized fractal dimensions (Dq), which correspond to scaling exponents for the q^{th} order of the measure can be defined by [88]:

$$D_q = \frac{1}{(q-1)} \lim_{\varepsilon \to 0} \frac{\log Z(q,\varepsilon)}{\log \varepsilon} = \frac{1}{(q-1)} \lim_{\varepsilon \to 0} \frac{\log \sum_{i=1}^{N(\varepsilon)} P_i^q(\varepsilon)}{\log \varepsilon} \quad \textbf{(8)}$$

if $q = 1$, to calculate the generalized fractal dimension D_1, we use:

$$D_1 = \lim_{\varepsilon \to 0} \frac{\sum_{i=1}^{N(\varepsilon)} P_i(\varepsilon)\, log P_i^q(\varepsilon)}{\log \varepsilon} \quad \textbf{(9)}$$

And, if $q = 0$, we have the so-called fractal dimension:

$$D_0 = \lim_{\varepsilon \to 0} \frac{\log Z(q,\varepsilon)}{\log \varepsilon} = \lim_{\varepsilon \to 0} \frac{\log \sum_{i=1}^{N(\varepsilon)} P_i^q(\varepsilon)}{\log \varepsilon} \quad \textbf{(10)}$$

and the mass exponent and it can be obtained by the following equation:

$$\tau(q) = \lim_{\varepsilon \to 0} \frac{\log Z(q,\varepsilon)}{\log \varepsilon} = \lim_{\varepsilon \to 0} \frac{\log \sum_{i=1}^{N(\varepsilon)} P_i^q(\varepsilon)}{\log \varepsilon} \quad \textbf{(11)}$$

Combining (8) and (11):

$$D_q = \frac{\tau(q)}{(q-1)} \quad \textbf{(12)}$$

Therefore, the multifractal spectrum function can be calculated by the Legendre transformation [88]:

$$f\big(\alpha(q)\big) = q\alpha(q) - \tau(q) \quad \textbf{(13)}$$

where $\alpha(q) = d\tau(q)/dq$. Dq and $\alpha(q)$ are calculated as the generalized dimension of Hölder exponents of q and provide information about fractal/multifractal geometry, while $f(\alpha)$ is related to the singularity spectrum [88,89].

.

3.4. ^{13}C NMR Spectroscopy

The high-resolution solid-state ^{13}C NMR experiments were performed on a Bruker® Avance 400 spectrometer, using a Bruker 4–mm Magic Angle Spinning (MAS) double resonance probe head, operating at 400.0 MHz (^{1}H) and 100.5 MHz (^{13}C) with 2.5 μs and 4.0 μs of π/2 pulse length, respectively. About 200 mg of powdered samples were packaged into 3.2 mm zirconia rotors and all spectra were recorded at (25 ± 1) °C. RF–ramped cross–polarization (^{13}C CPMAS) [90] and Spinal–16 high power ^{1}H decoupling [91] performed with γB1/2π =70 kHz nutation frequency were applied for ^{13}C signal acquisition. The acquisition parameters were set as 5 s of recycle delay, 40 ms of acquisition time and 1024 scans.

3.5. Computational Method

Since the ^{13}C NMR Spectroscopy results indicated the existence of head–to–tail (HT) as well as head–to–head (HH) polymerization for PPA, geometry optimizations were performed for both forms of PPA polymer structures (labeled as PPA_{HT} and PPA_{HH}) using quantum-chemical Density Functional Theory [92] as implemented in the Gaussian 03 program package [93]. In particular, the gradient-corrected correlation functional of Perdew, Burke and Ernzerhof (PBE) [94,95] in combination with the 6-311G(d,p) basis set was utilized for this purpose. Both PPA_{HT} and PPA_{HH} are tetramers formed out of covalent bonding of the four *p*-anisidine monomers in the conformation of the polymer chain. The doped forms of PPA were also considered (labeled as Cl–PPA_{HT} and Cl–PPA_{HH}). Harmonic vibrational frequencies were determined for each optimized geometry at the same level of theory and positive frequencies were found for all vibrational modes in each optimized PPA to guarantee the obtention of a local minimum on the potential energy hypersurface. Preparation of the initial molecular structures and partial analysis of the calculated results were done with the aid of Gaussview program [96].

3.6. FTIR Analysis

FTIR spectra were recorded using a Shimadzu IR Prestige–21 Spectrometer TA Instruments® from 4,000 cm^{-1} to 400 cm^{-1}, resolution of 1 cm^{-1} and 64 scans.

3.7. Electrical Conductivity

A Solartron 1260 impedance analyzer was used for collecting data at 27 °C by applying 500 mV from 10 Hz to 1 MHz. Polymers were pellet (1.3 cm in diameter and 0.14 cm in thickness) without thermal treatment and conductive ink exposure.

4. RESULTS AND DISCUSSION

4.1. Percentage of Crystallinity and XRD Analysis

PPA were synthesized according to the experimental conditions described in **Table 1**. A number of 17 syntheses were performed (from PPA1 to PPA17) based on the CCRD method. However, the polymerization of PPA11 was not observed.

The crystalline state is based on a 3D positional and orientational order. Continued growth of the crystalline polymer phase would result in large scale polymerization with polymer crystals lying in certain preferred directions [52]. In polymer crystals the macromolecules are longer than the unit cell parameters and each polymer chain is supposed to pass through several unit cells. For this reason, general requirements for the nucleation and growth of crystalline phase of polymers are based on the regularity in the chemical constitution, as well as in the configuration of long sequences of monomeric units [97]. The conformation of the polymer chains in the crystalline state depends on the configuration of the stereoisomeric centers present along the chains, and it is based on the principles of equivalence and of minimum internal conformational energy [98].

The three-dimensional long-range order is never present in polymer crystals and the structural disorder inside is a rule rather than an exception [97]. For this reason, the crystallinity concept in polymeric materials is significantly complex, being considered as semicrystalline materials generally composed of crystals (lamellae) embedded into a non-crystalline phase, resulting in a highly interconnected network [98]. The verification of the existence of crystalline regions in polymeric materials became more evident from the 1920s, when some polymers subjected to XRD analysis presented characteristic peaks (previously observed only in crystalline materials). These peaks appeared in addition to a diffuse halo (as observed in XRD patterns of liquids), also pointing to the presence of a non-crystalline

contribution from the same material. This verification allowed the confirmation of the coexistence between the crystalline and non-crystalline phases in polymeric materials.

The percentage of crystallinity of polymeric materials is then related to the amount of the crystalline contribution in the entire material. An absolute value is not possible to be obtained because it depends on the technique used to estimate crystallinity [99]. Furthermore, several parameters and synthesis methodology influence on the polymer crystallinity, so a range of percentage of crystallinity can be obtained for a specific polymer [48].

Herein, the calculation of the percentage of crystallinity of each *as*-synthesized PPA was based on the separation and quantification of the integrated intensities from the semi crystalline (PPA1 and PPA16) and non-crystalline (heat-treated PPA1) phases. This method is based on the obtainment of an internal diffraction pattern of the same sample in the non-crystalline state [12,100]. A completely non-crystalline polymer of the same chemical composition can be used as a standard for estimating the percentage of crystallinity [101]. This non-crystalline pattern can often be obtained by heat treatment or other methodology resulting in a non-crystalline material. Considering conjugated polymers, the acid-base neutralization reactions were previously reported [12]. The separation and quantification of the integrated intensities from a semi crystalline to calculate the percentage of crystallinity of polymer materials were previously reported elsewhere [12,102].

The effect of the concentration of monomer, APS and HCl on the percentages of crystallinity of each PPA sample was considered. The treatments performed experimentally resulted on different crystal structures due to the combination of different amounts of reagents applied in each chemical oxidative polymerization, giving rise to 16 different XRD patterns (data not shown). The percentage of crystallinity ranged from (29.2 ± 0.6) % to (55.1 ± 0.2) %.

Fig. 10 shows the semi crystalline XRD patterns of the *as*-synthesized PPA1 and PPA16 as a consequence of some polymer chain alignment. However, broad peaks are due to the nanosized crystalline phase (crystallites), which coexist in a non-crystalline phase.

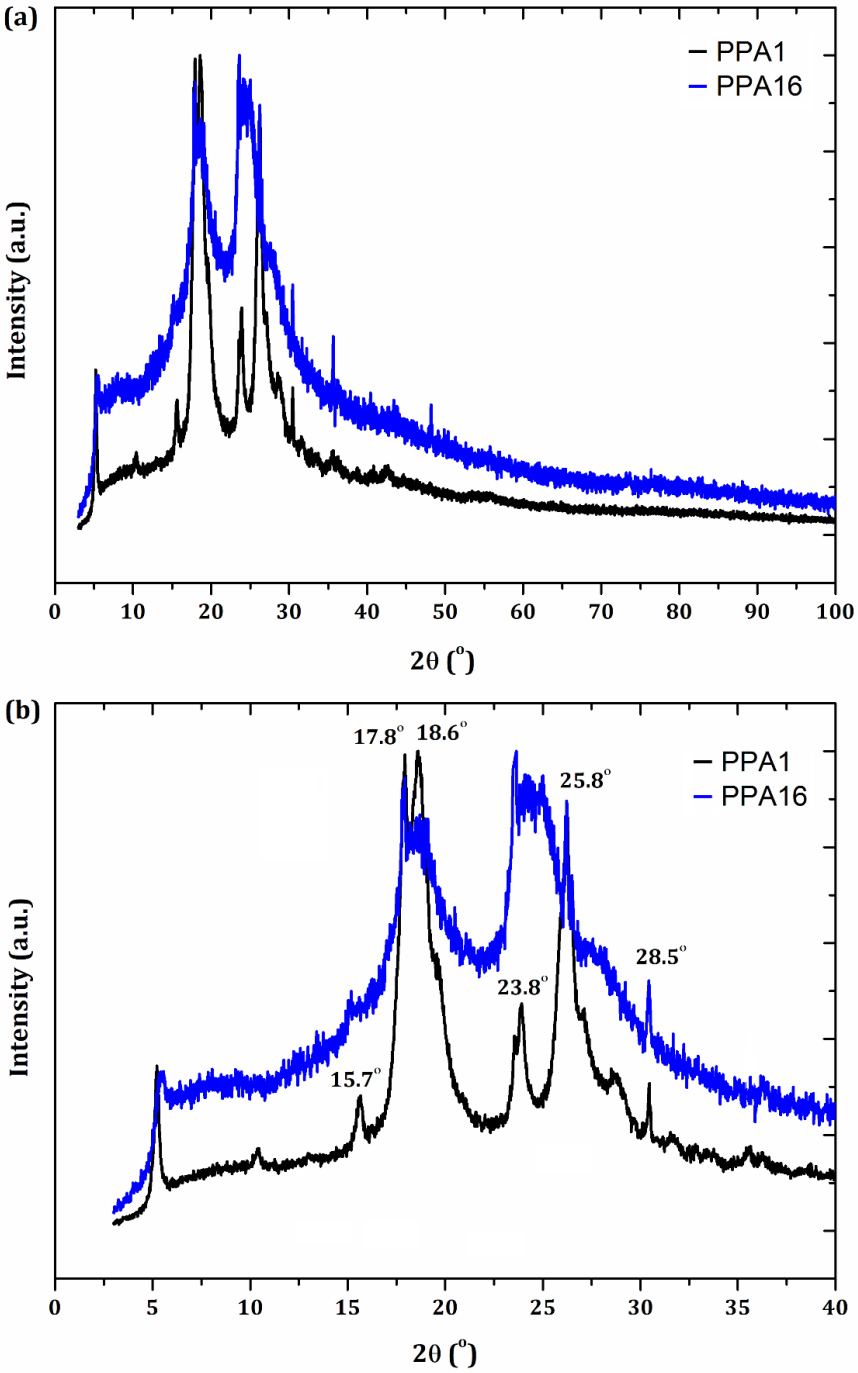

Figure 10. Semi crystalline XRD patterns of the (a) as-synthesized PPA and (b) the angular region 2θ = 3° – 40° highlighting the most intense diffraction peak positions.

The scientific literature reported that several factors influence on the crystallinity and polymerization of polyaniline and its derivatives. These factors are related to *(i)* the different synthesis methodologies [38,103,104], *(ii)* the regular packing of the polymer chains, *(iii)* the ring side group at the *ortho*, *meta* or *para* positions [30,105–107], *(iv)* the nature of the doping

acid and counterion size [32], as well as *(v)* possible chemical or physical interactions between counterions and the ring side group [7]. Our results showed that the doping acid concentration presented the greatest effect on the percentage of crystallinity of PPA, followed by the *p*-anisidine monomer and APS. Then, only the polymers showing the highest (PPA1) and lowest (PPA16) percentage of crystallinity were selected for further analysis.

The XRD patterns of PPA1 and PPA16 are clearly correlated. Both patterns present an intense peak at 2θ = 5.2° (*d* = 16.9 Å). However, the peak of PPA1 is significantly narrow, probably due to the presence of larger crystallites. On the other hand, a broad hallo in the PPA16 pattern from 2θ = 10.0° – 30.0° suggests reduced crystallinity. PPA1 and PPA16 also present a small peak at 2θ = 15.7° (*d* = 5.6 Å), as well as a broad peak at 2θ = 28.5° (*d* = 3.1 Å).

The XRD pattern of PPA16 also shows two broad and intense peaks: the first one was found from 2θ = 16.5° to 21.0°, centered at 2θ = 18.5° (*d* = 4.8 Å); the second broad peak ranged from 2θ = 22.5° to 26.7°, centered at 2θ = 24.5° (*d* = 3.6 Å). The XRD of PPA1 sample also showed peaks at the same angular region as that of PPA16, however, they are much more defined as can be observed from Fig. 1(b). Around the center of the first PPA16 peak (2θ = 18.5°) appeared two sharp peaks of PPA1 – one at 2θ = 17.8° (*d* = 5.0 Å) and another at 2θ = 18.6° (*d* = 4.8 Å). On the other hand, at around 2θ = 24.5° (center of the second PPA16 peak) PPA1 presented three well defined peaks at 2θ = 23.8° (*d* = 3.7 Å), 25.8° (*d* = 3.4 Å) and 27.1° (*d* = 3.3 Å). Our results clearly showed an improved crystallinity in PPA1 as a consequence of the synthesis conditions such as the reagent concentrations.

There is a lack of structural reports on PPA in the literature. Hybrid materials based on PPA and clay were reported [108]. The formation of nanomaterials was confirmed by XRD results demonstrating the intercalation of PPA into the clay phase by accessing increased interlayer spacing. The semi crystalline XRD patterns of the pure PPA presented peaks at 2θ = 3.58°, 7.38°, and 24.35°, which is significantly different from that presented in the present study. The authors used $HClO_4$ as dopant acid, which may result in a different PPA crystal

structure. The nature of the dopant acids significantly influences on polymerization and crystallinity of conjugated polymers [7,109]. Moreover, the XRD pattern of polymeric blends of PPA and ZnO nanoparticles was also reported [14]. Despite presenting XRD pattern similar to that of PPA16, the authors did not provide the angular positions of the pure PPA peaks. In addition, the XRD measurements started at 2θ = 10°, preventing the confirmation of the intense and narrow peak observed here at 2θ = 5.2°.

4.2. Morphological Evaluation

Scanning Probe Microscopy (SPM), such as Scanning Tunneling Microscopy (STM), Atomic Force Microscopy (AFM) and even profilometry, are techniques based on the production of three-dimensional images of surfaces, which are suitable for the study of fractal properties. However, the images produced by Scanning Electron Microscopy (SEM) have also been widely used in fractal and multifractal analysis of surfaces [110], providing two-dimensional images without information on the height profile. In this case, the SEM image of a fractal surface is not self-similar in all spatial directions and presents the advantage of not introducing the tip convolution effect (usually causing a systematic error in the estimative of the fractal dimension surface) [111]. **Fig. 11** shows the SEM images of (a-c) $PPA1_{HT}$ and (d-f) $PPA16_{HT\text{-}HH}$.

Basically, two types of morphology are observed in both samples: needles and globular particles. As previously observed in the XRD results, the diffractograms are typical of semi crystalline materials, and narrow peaks are observed superimposed on a diffuse pattern. The SEM images suggest that the needle phase may be related to the crystalline contribution of the polymer on the XRD patterns. These data become more consistent because the number of needles decreases in the $PPA16_{HT\text{-}HH}$ sample, which also present a lower percentage of

crystallinity. On the other hand, according to the SEM images, the decrease in the percentage of crystallinity is accompanied by the increase in globular morphology.

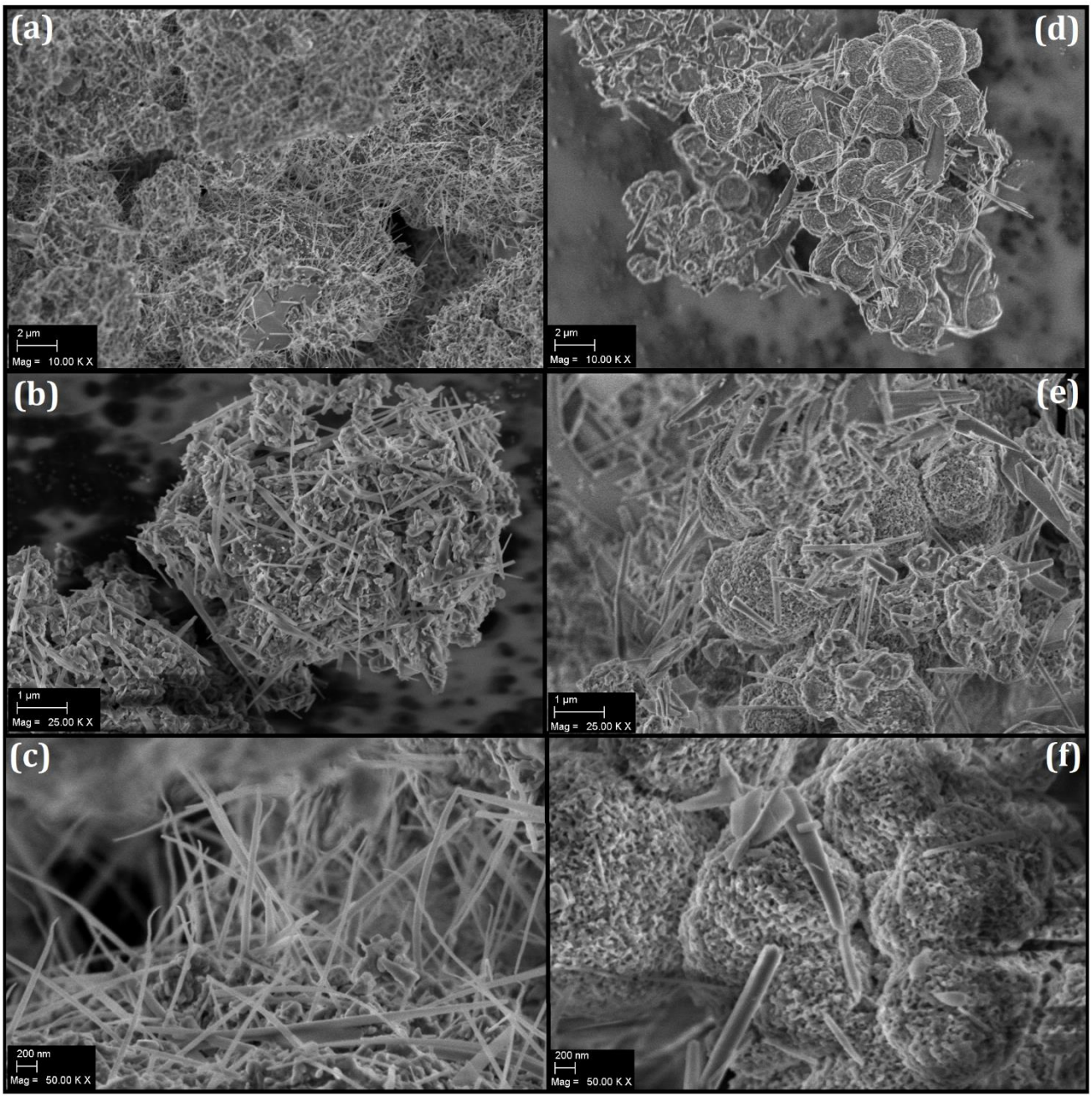

The SEM technique has the main advantage of generating images with a high pixel density due to its high resolution of 1,024 x 768 pixels. **Fig. 12** shows the SEM micrographs (with magnifications of 25,000x and 50,000x) of PPA highlighting the influence of the synthesis parameters and concentration on the polymer's morphology.

Fig. 12(a) shows that the surface basically formed by elongated needles (up to a few microns in length), pointing to a polymer growth direction. At higher magnification [**Fig. 12(a)**, right] and applying a lighter contrast image, some roughness is also observed. On the other hand, **Fig. 12(b)** demonstrates a significant change in morphology when compared to that of **Fig. 12(a)**. The elongated needles are present in reduced amount, while the globular morphology increases considerably presenting larger globules. In addition, the needles seem to be wider and shorter.

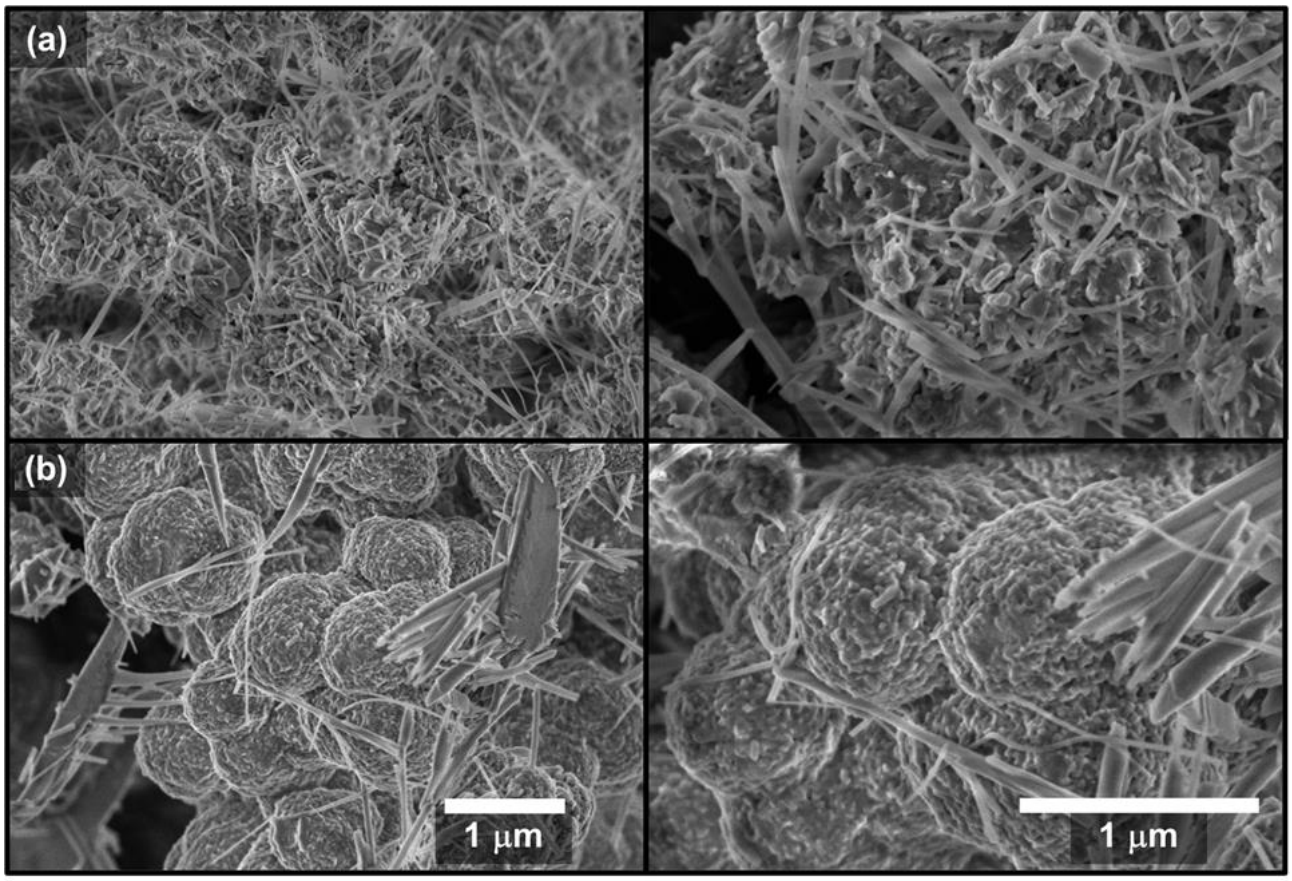

Figure 12. SEM micrographs of (a) PPA1$_{HT}$ and (b) PPA16$_{HH\text{-}HH}$. Magnification of 25,000x and 50,000x.

The SEM images are provided in grayscale, allowing a good indirect method by using a color gradient across the entire image. In this case, the black color represents the lowered area, the white color indicates the raised area, and the gray color (in various intensity levels) represents the height between the lowered and raised levels. Therefore, the relative elevation

value of each point in the range of 0 to 255 for each gray value at each point in the SEM image was obtained [112].

For this reason, **Fig. 12** (with the magnifications of 50,000x) has been enlarged in specific regions using the software Gwyddion 2.59 [113]. Thus, **Fig. 13 (a-b)** show the 2D and 3D reconstructions, with 3.7 mm x 3.7 mm squared areas, in which colors are used to highlight the differences between both samples. The *z*-axis of the 3D images does not have a metric dimension, and it just denotes the intensity variation of the gray levels of the original SEM images. These images have been used for the multifractal study presented herein.

4.2.1. Multifractal Analysis

Digitized images (such as those provided by the SEM technique) can be used to obtain relevant quantitative surface information of a wide range of micro and nanostructures through fractal analysis. The fractal dimension D (for 3D objects, $2 \leq D \leq 3$) presenting higher values indicates substantial geometric details and irregularities. The multifractal analysis performed in this work represents a generalization of the fractal approach and can provide a more comprehensive description of fractal surfaces [114].

Multifractal analysis describes the local behavior of measurements or functions in a geometrical and statistical method. Using the classical formalism of multifractal analysis, a spectrum of fractal dimensions (multifractal spectrum) can be obtained. Multifractality is used in the description of heterogeneous systems consisting of subsets exhibiting local self-similar properties, based on the concept of self-similarity, requiring the introduction of a probability measurements [115].

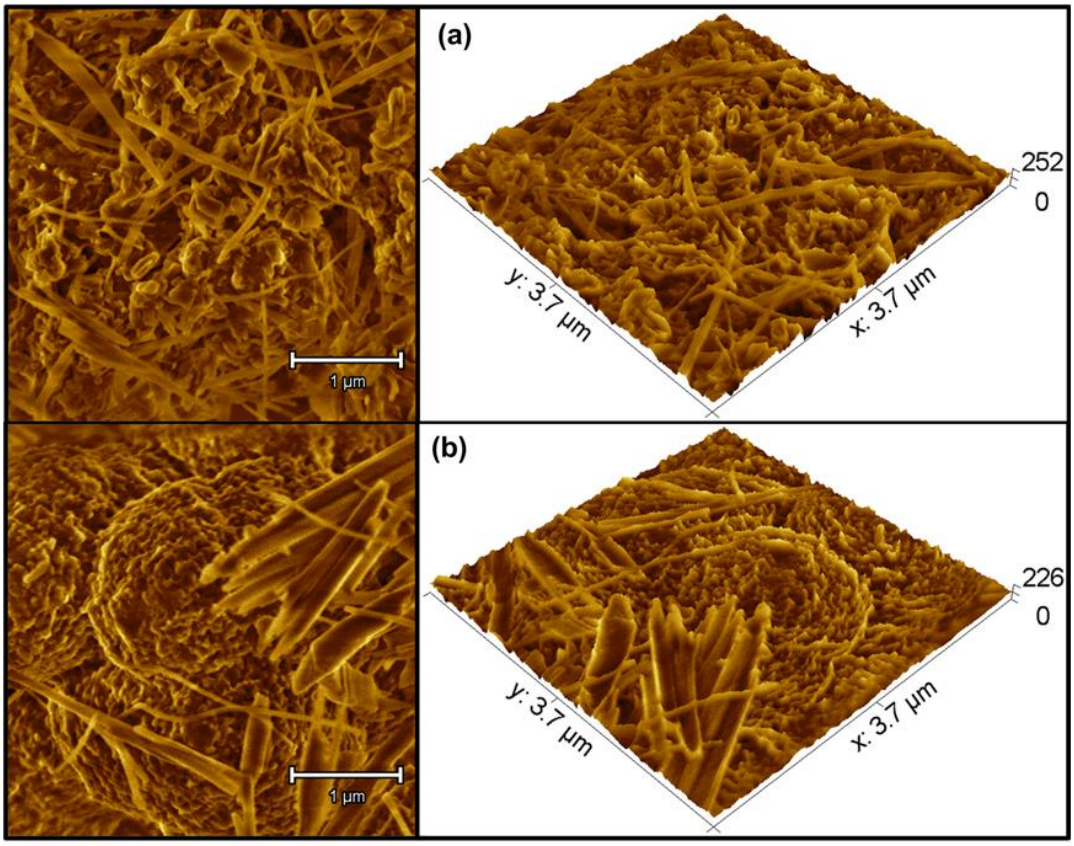

Figure 13. 2D and 3D zoom reconstructions of SEM images (50,000x) from (a) $PPA1_{HT}$, (b) $PPA16_{HT\text{-}HH}$.

Fig. 14 shows the results obtained of the multifractal analysis of the images from **Fig. 13**. The mass exponent (τ) as a function of the moment of order (q) [**Fig 14(a)**] indicates that both $PPA1_{HT}$ and $PPA16_{HT\text{-}HH}$ present a non-linear tendency, as well as a multifractal behavior which is more evident in $PPA1_{HT}$.

The evidence of multifractality is supported by the non-constant behavior of Dq *versus* q [**Fig. 14 (b)**], as well as by the concave curve of the multifractal spectrum $f(\alpha)$ *versus* α, shown in **Fig. 14 (c)**. The τ and Dq parameters were calculated for different moment values (q) in a range of $-15 < q < 15$. As observed in **Fig 14,** $PPA1_{HT}$ clearly exhibits distinct characteristics, that are confirmed by the estimated parameters related to the multifractal spectra presented in **Table 2**. The parameter Δf represents the difference of fractal dimensions between maximum and minimum singularity strength being calculated by $\Delta f = f(\alpha_{min}) - f(\alpha_{max})$, quantifying, in this way, the strength of multifractality [59]. Thus, the analyzed surface is dominated by areas described by a high probability value when $\Delta f > 0$. However, when $\Delta f < 0$

the dominant areas are described by their low probability value. If Δf is significantly small, the height distribution of the mass deposited at the highest site is equal to that at the lowest sites, indicating more homogeneous structures [60]. On the other hand, a greater variation of f indicates greater heterogeneity of the analyzed structure [61]. **Fig. 14(c)** shows the shape and extent of the multifractal spectrum *f(a) versus a*, where the asymmetry of the distribution indicates the presence of multifractal. According to **Table 2**, in both $PPA1_{HT}$ and $PPA16_{HT\text{-}HH}$the Δf values are similarly positive, being higher in $PPA1_{HT}$. The singularity spectrum is wider for $PPA1_{HT}$ due to greater surface heterogeneity and percentage of crystallinity (as previously observed on the XRD results). In addition, the spectrum is shifted to higher values and the multifractal spectrum of $PPA1_{HT}$ shows a greater inclination to the right when compared to that of $PPA16_{HT\text{-}HH}$. Our results shows that the surface becomes more irregular and complex when the crystallinity is reduced. As a consequence, higher values of the multifractality parameter *Da* are observed, while the $\Delta f(a)$ values are reduced. It can be observed from **Fig. 14(c)** and **Table 2** that $PPA1_{HT}$ presents the greatest $\Delta\alpha$ width spectrum, pointing to the highest degree of multifractality.

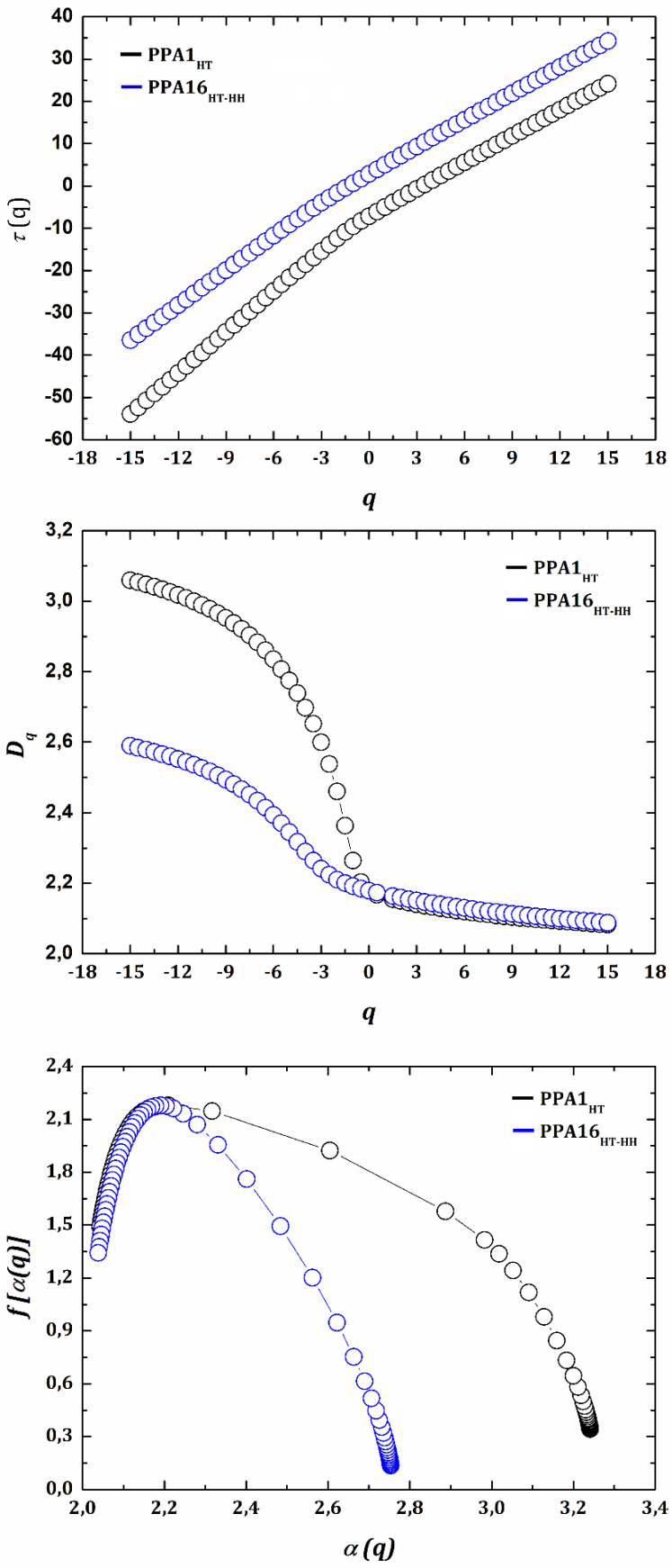

Figure 14. (a) Mass exponent τ(q), (b) generalized dimensions Dq and (c) Multifractal spectra [$f(\alpha)$ *versus* α] as a function of the order of moments computed for PPA1$_{HT}$ and PPA16$_{HT\text{-}HH}$.

Table 2. Parameters from the multifractal spectra.

Parameters	PPA1$_{HT}$	PPA16$_{HT\text{-}HH}$
$f(\alpha_{max})$	0.34	0.14
$f(\alpha_{min})$	1.49	1.34
Δf	1.15	1.20
α_{max}	3.24	2.75
α_{min}	2.04	2.04
$\Delta\alpha$	1.20	0.71

Systematic structural studies have been performed using the AFM technique to describe statistical parameters used to evaluate the complexity of an individual surface [119,120]. This technique allows the understanding of the influence of the material surface on specific properties, such as controlled released of biomaterials. As a result, statistical parameters related to the nanoparticles surface, such as roughness, peak distribution, height distribution and nanotexture homogeneity have been determined. A previous report [119] presented an advanced morphological and fractal aspects of polymeric particles surface containing encapsulated essential oil, which were evaluated using AFM topographical images. The authors pointed to the influence of the essential oil concentration on the particle's morphology and surface roughness. This tool can be useful to evaluate the quality standard in the development of novel materials for controlled release of bioactive compounds.

A 3D nanoscale morphological surface analysis of polymeric particles containing different concentrations of bioactive compound was proposed elsewhere [120]. The author verified that higher concentrations of bioactive compound promoted a decrease in the dominant spatial frequencies of the particle surfaces. The proposed evaluation allowed to access stereometric parameters, which can be a guide in the development of novel particle

carriers with desirable surface properties for technological application based on microtexture roughness.

The fractal dimension calculations have also been performed for conjugated polymers [121]. Poly(*o*-methoxyaniline) emeraldine-salt form (ES–POMA) was subjected to a heat treatment process, promoting a progressive reduction of crystallinity. SEM images was obtained to show the micromorphology changed induced by heating, resulting in loss of globular morphology. Parameters based on statistical data allowing the morphology and geometric structure characterization were accessed. The untreated ES-POMA presented a greater distribution of heights; however, the heat-treated polymers exhibited a considerably reduced symmetrical behavior. The authors verified that the polymer presented a significant morphological change after the heating process (also based on Df values), pointing to smoother surfaces with smaller height variations.

4.3. ^{13}C NMR Spectroscopy

The isomeric positions of anisidines (*meta*, *ortho* or *para*) result in different ^{13}C NMR spectra as the chemical environments of the carbon atoms (arrangements of neighboring nuclei) are also different [122]. These spectra are useful to estimate the positions of the methoxy and amine groups, as well as other carbon atom positions.

Fig. 15 shows the non-normalized high-resolution solid state ^{13}C NMR spectra of PPA1 and PPA16. The ^{13}C NMR spectra observed in solid-state, even using magic-angle sample spinning (MAS) show broader signals than the ^{13}C NMR spectra recorded in solution due to the residual anisotropic effects (dipolar coupling) that responds to the conformational changes, which regards from differences on intramolecular interaction. The chemical shift signals between δ = (135–120) ppm observed in the PPA16 spectrum were more overlapped and less

defined, suggesting larger non-crystalline content. This result was previously observed from the XRD results.

The observed absence of signals centered at 173.9 ppm, 143.7 ppm and 102.0 ppm in the PPA1 spectrum suggests a more regular crystal structure. In polymer materials, signals with a spectral profile similar to another next neighbor probably indicate similar molecular structure, but in different positions or spatial arrangements. For this reason, our results suggest two different types of polymerizations: head–to–tail (PPA_{HT}) and head–to–head (PPA_{HH}) polymer chains.

The proposition of the molecular polymerization of PPA requires an understanding of the electron density distribution of aromatic rings. The methyl group is not allowed to participate of the polymerization process due to the mechanisms of proton loss/suppression or hydride migration. On the other hand, proton loss is highly improbable since the formed carbanion is significantly reactive.

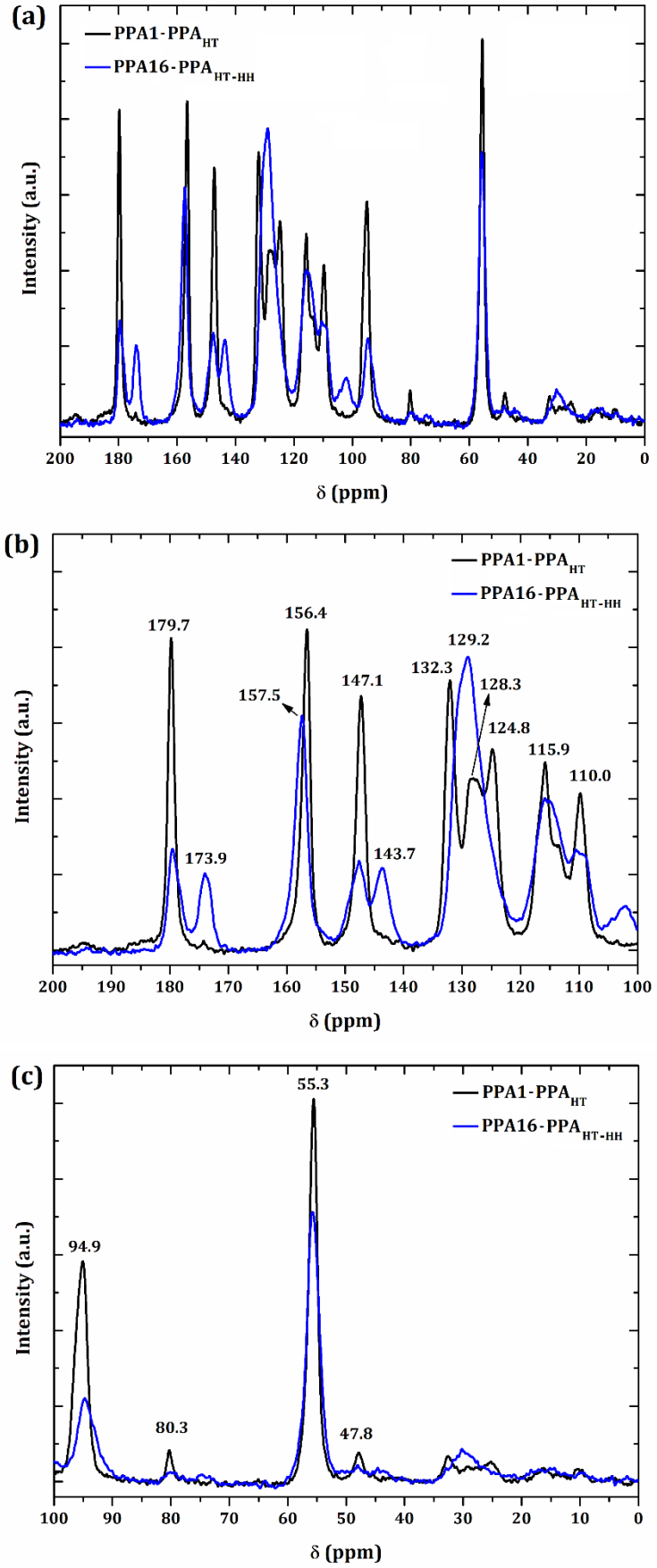

Figure 15. 13C NMR spectra of PPA1$_{HT}$ and PPA16$_{HT-HH}$ (a) δ = (200 – 0) ppm, (b) δ = (200 – 100) ppm and (c) δ = (100 – 0) ppm.

As the reaction started from the *p*-anisidine monomer, only the amine group and the *ortho* and *meta* positions can participate of the polymerization. The amino and carboxy groups are known to be a ring activating groups, "increasing" the electron density at the respective *ortho* and *para* positions, and "decreasing" the electron density of the respective *meta* positions.

This result indicates that the *ortho* and *para* positions became more electronically negative, and the opposite effect is expected for the *meta* position. However, due to the molecular symmetry, the *ortho* position of one group is the *meta* position of the other group. In this case, the amine group is more activating than the methoxy group, so the *meta* position related to the amine is "more positive" than that of *meta* position related to the methoxy group. Similarly, the *ortho* position related to the amine group is "more negative" than that of methoxy group.

Solid-state polymerizations can generally be regarded as phase transitions from the crystalline phase of the monomer to the polymer growth phase. The character of these phase transitions determines the mechanism of the polymerization. It is, therefore, necessary to know the mechanism of 3D order of the crystalline monomer transferred to the resulting polymer phase [52]. Our results suggest that the polymerization reaction started from both the non-bonding electrons of the amine groups and oxygen atom. Thus, the bonds between these groups should not be considered, since the N–O, O–O and N–N bonds are extremely unstable and photosensitive. The oxygen atoms do not find a more energetically stable situation for polymerization. What remains, in fact, is the bond between the amine groups and the carbon atoms in the *ortho* and *meta* positions. At this point, there are two possible considerations: *(i)* in the first situation (head–to–tail PPA), the amine group is bonded at the *meta*–position of the amine from the neighboring residue through its non-bonding electrons. This polymerization pathway is considerably relevant because this carbon atom is the "most positive" of the aromatic ring; *(ii)* as both carbon atoms (*ortho* and *meta*) are influenced by the amine and

methoxy groups, the bond with other carbon atoms can also occur, but to a lesser extent, resulting in a head–to–head (PPA_{HH}) molecular structure.

The morphology and texture of a solid-state polymer results from a overall reaction as the primary molecular structure. Thus, the knowledge of the crystal structure of the monomer as well as the molecular structure and morphology of the as-synthesized polymer is important to explain the solid-state polymerization mechanism [52]. A detailed picture of the reaction mechanism of PPA is still very difficult to develop. However, the assignment of the solid state ^{13}C NMR signals of the carbon atoms of the PPA_{HT} and PPA_{HH} molecular structures, based on the concept of electronic shielding, was useful. The electronic cloud field is vectorially opposed to that applied by the equipment. The denser this cloud (greater number of electrons), the greater is the shielding from the external field. High electron density usually means greater polarization of the nuclei and lower upfield shifted frequencies. However, the opposite situation is also considered, resulting in signals further downfield shifted frequencies. Therefore, the signals from the methoxy carbon are intense, highly polarized and located far to the right of the spectrum.

The signals at 94.9 ppm and 102.0 ppm are assigned to an isolated carbon between the functional groups of the molecular structure. As mentioned before, the amine group activates the *ortho* position, so two amines still activate more than one amine and one methoxy group. For this reason, a signal separation (94.9 ppm and 102.0 ppm) was observed suggesting that the head-to-tail molecular structure was predominant in PPA1. Similar results are observed in the signals at 147.1 ppm and 143.7 ppm. In this case, as one amine is located at the *meta* position relative to another in a head-to-tail molecule, the carbon core is slightly deshielded when compared to the same core in the head-to-head molecule (where the amine groups are located at *ortho* position to each other). Another evidence of these molecular structures is related to the signals at 179.7 ppm and 173.9 ppm based on the same interpretation. However, these

signals were not found in the monomer spectrum [122], indicating an effective polymerization/conjugation due to the presence of –N= bonds.

The proposed molecular structures of PPA_{HT} and PPA_{HH} are shown in **Fig. 16**. Furthermore, the spectra signals were useful to estimate the percentage of head–to–tail and head–to–head molecular structures: PPA1 was fully (100 %) constituted of head–to–tail polymer chains (PPA_{HT}), while PPA16 was formed predominantly by head–to–tail molecular structure [(62.0 ± 0.5) %; $PPA_{HT\text{-}HH}$).

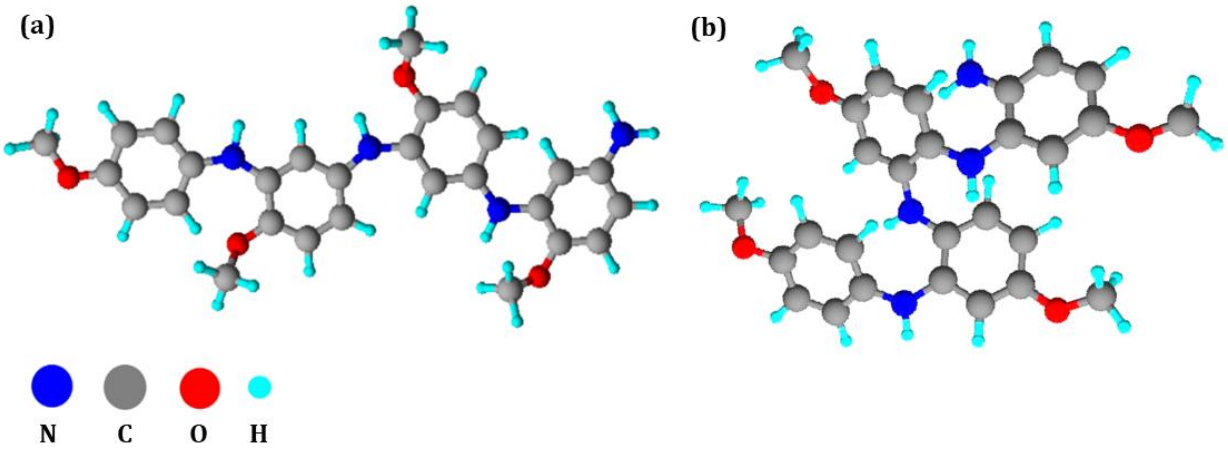

Figure 16. Proposed molecular structures of PPA_{HT} and PPA_{HH} from 13C NMR results.

The structure of a polymer network is normally determined by polymer chains of different lengths, which are disordered in a random orientation [9]. Our results suggest that the homogeneity of the head–to–tail polymerization of PPA resulted in enhanced percentage of crystallinity, as shown in the XRD and ^{13}C NMR results. A combination of head–to–tail and head–to–head polymer chains influenced on the amount of non-crystalline phase. On the other hand, the concentration of *p*-anisidine monomer, APS and HCl also affected the mechanism of polymerization, and their lower concentration favored a more crystalline, homogeneous head–to–tail polymerization.

4.4. Geometry Optimization

The quantum-chemical investigation of the molecular structure of PPA has been carried out through the geometry optimization of the head–to–tail (PPA_{HT}) and head–to–head (PPA_{HH}) tetramers in the ground state. The optimization has also been performed for the molecular structures of the chlorine doped PPA. The Cl^- counter ion was incorporated into the molecular structure of PPA_{HT} and PPA_{HH} to obtain the doped polymer Cl–PPA_{HT} and Cl–PPA_{HH} respectively. **Fig. 17** shows the PPA_{HT}, Cl–PPA_{HT}, PPA_{HH} and Cl–PPA_{HH} tetramers and their respective molecular dimensions and energy values.

The molecular structures of the doped tetramers presented different dimensions: the *x*–dimension increased, the *y*–axis was reduced and the *z*–lattice presented marginal modification.

Polyaniline and its derivatives can present some degree of molecular organization, resulting in a semi-crystalline crystal structure. However, the doping process significantly influences the arrangement of the polymer chains [48]. Doped conducting poly(*o*-methoxyaniline) presented percentage of crystallinity ranging from 48 % to 63 % as a function of the time of polymerization. However, after the neutralization process to obtain its undoped form, the crystallinity was reduced to 27 %, showing the influence of the counter ions on the molecular chains alignment [10,11]. Charged nanoparticles can also influence on the alignment of conducting polymer chains [56]: gold nanoparticles stabilized with sodium citrate was able to form a complex with polyaniline emeraldine-salt form, reducing considerably the percentage of crystallinity of the resulting material.

Doped conducting polymers usually present higher percentage of crystallinity and electrical conductivity. Furthermore, the head–to–tail and head–to–head polymerization (or their combination as observed in $PPA16_{HT\text{-}HH}$) can result in particular electronic properties controlled both by bond length and torsional angle dimerization, since the phenylene rings

move from the plane defined by the nitrogen atoms to reduce the strong sterical hindrance [123]. As shown in **Fig. 17**, these torsions are considerable different in PPA_{HT}, $Cl–PPA_{HT}$, PPA_{HH} and $Cl–PPA_{HH}$ structures, and can influence on the delocalization and mobility of the charge carriers.

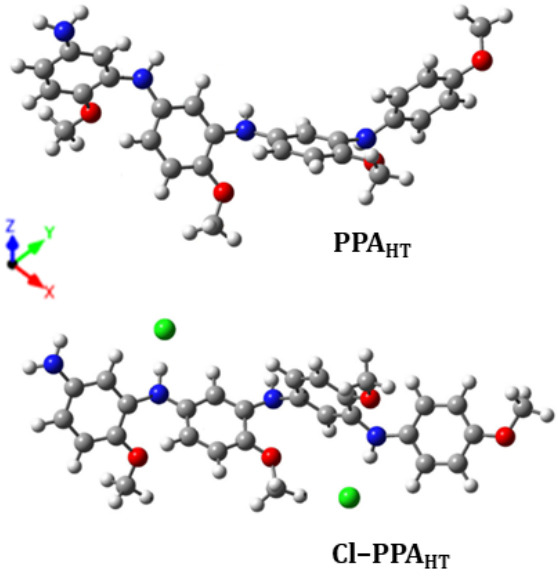

Molecular Dimension	Energy (Hartree)
PPA_{HT}	
R_x = 21.086	
R_y = 10.233	−1603.329
R_z = 7.374	
$Cl–PPA_{HT}$	
R_x = 22.785	
R_y = 8.834	−2523.379
R_z = 6.109	

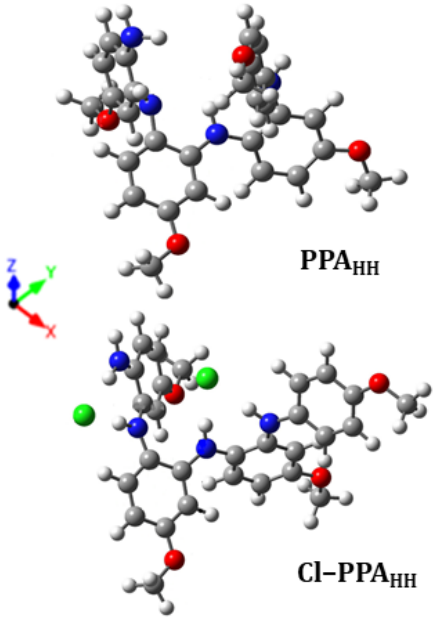

Molecular Dimension	Energy (Hartree)
PPA_{HH}	
R_x = 13.617	
R_y = 13.522	−1603.349
R_z = 11.114	
$Cl–PPA_{HH}$	
R_x = 14.939	
R_y = 11.416	−2523.421
R_z = 11.384	

Figure 17. PPA_{HT}, $Cl–PPA_{HT}$, PPA_{HH} and $Cl–PPA_{HH}$ tetramers and their respective molecular dimensions and energy values after relaxation.

After evaluating the influence of the counter ions on the molecular dimensions and energy values of PPA$_{HT}$, Cl–PPA$_{HT}$, PPA$_{HH}$ and Cl–PPA$_{HH}$ tetramers, a monomer from each polymer is structurally characterized in **Fig. 18** (a–d) with the interatomic distances being labelled by d_n $(n = 1 - 11)$.

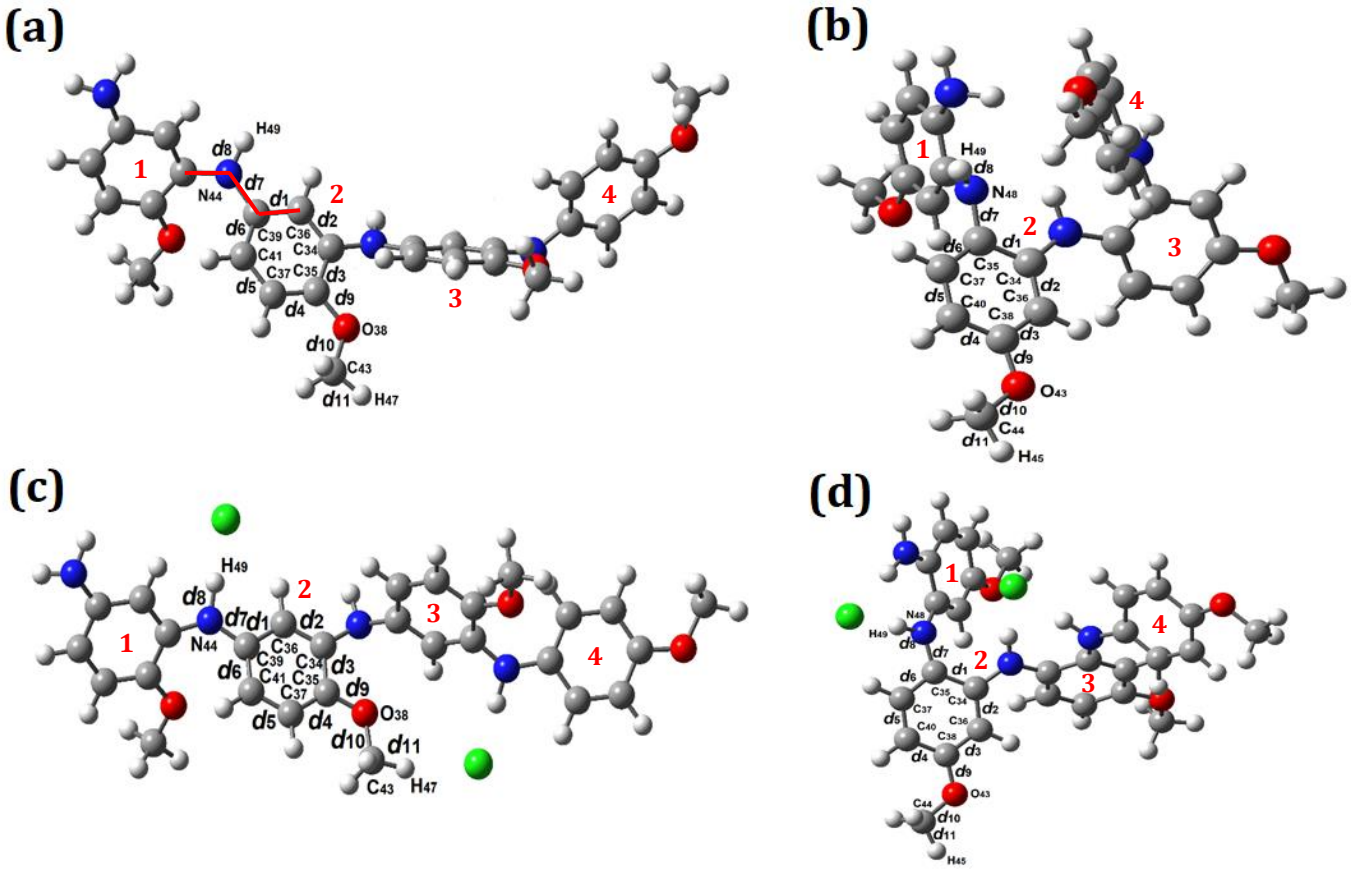

Figure 18. Geometric optimization of PPA$_{HT}$, Cl–PPA$_{HT}$, PPA$_{HH}$ and Cl–PPA$_{HH}$ tetramers. (a) undoped PPA$_{HT}$, (b) undoped PPA$_{HH}$, (c) doped Cl–PPA$_{HT}$ and (d) doped Cl–PPA$_{HH}$. Interatomic distances were identified from d_1 to d_{11}.

The presence of counter ions allows greater regularity to the polymer tretramer when compared to the undoped systems. Differences were observed between the dihedral angles measured between two rings, as highlighted in red in **Figure 18**, comparing the doped systems with their respective undoped systems. The angles between the rings 1–2, 2–3 and 3–4 of the PPA$_{HT}$ structures (**Figure 18 (a,c)**) changed by 6.70°, 65.13° and 10.07°, respectively. The largest difference is found in the angle related to the 2–3 rings, which is the region presenting

the greatest interaction between counter ions and polymer chain. The absence of counter ion–chain interactions in the undoped system increases the freedom of rotation of the repetitive unit, twisting the chain towards a shape tending to the spherical conformation.

Considering the PPA_{HH} structures **(Figure 18 (b,d))**, the greatest difference in the dihedral angles was observed in relation to the end of the polymeric chain. The rings 1–2 and 3–4 showed differences of 95.35° and 101.35° when the doped systems were compared to their respective undoped ones. The rotation of the ring 1 with respect to 2 was clearly observed after doping, as well as the rotation of the ring 4 with respect to 3. For this reason, it is concluded that counterions, in addition to modifying the electronic structure, directly influence the structural configuration of the polymer chains.

Table 3 shows the interatomic distances from d_1 to d_{11} highlighted in **Fig. 18**. Despite presenting two possible mechanisms of polymerization (head–to–tail and head–to–head), the resulting polymer molecules (PPA_{HT} and PPA_{HH}) do not present significant differences in interatomic distances and angle values. The angles at the carbon ring–bonded nitrogen atoms are almost similar in both types of polymerizations (for PPA_{HT}: $d_2 \leftrightarrow d_3$ = 30.881° and $d_1 \leftrightarrow d_6$ = 30.881°; for PPA_{HH}: $d_1 \leftrightarrow d_2$ = 30.386° and $d_1 \leftrightarrow d_6$ = 30.695°), revealing that the phenyl ring torsions are not considerably influenced by the type of polymerization.

The doped tetramers (Cl–PPA_{HT} and Cl–PPA_{HH}) show small variations in interatomic distances and angle values in the planes of the highlighted monomers, showing that doping process does not cause significant structural changes. However, the d_8 (N — H bond) values of both Cl–PPA_{HT} and Cl–PPA_{HH} have increased, respectively, from 1.016 Å to 1.101 Å and from 1.023 Å to 1.076 Å. These appreciable increments of N — H interatomic distances reveal the local influence of the counter ions on the molecular structures which might be the protonation of the hydrogen atom. The protonation process preferentially occurs at the imine nitrogen atoms followed by an internal redox reaction resulting in a semiquinone segment [124,125].

Table 2. Interatomic distances (Å) and angle values observed in PPAHT, Cl–PPAHT, PPAHH and Cl–PPAHH tetramers.

PPA$_{HT}$		**PPA$_{HH}$**	
Interatomic Distances (Å)	**Angles (°)**	**Interatomic Distances (Å)**	**Angles (°)**
d_1 = 1.407	(N_{44} C_{39} C_{36}) = 118.280	d_1 = 1.431	(N_{48} C_{35} C_{34}) = 118.103
d_2 = 1.400	(C_{35} O_{38} C_{43}) = 117.437	d_2 = 1.403	(C_{38} O_{43} C_{44}) = 117.364
d_3 =1.421	(C_{36} C_{39} C_{34}) = 28.816	d_3 = 1.405	(C_{34} C_{35} C_{36}) = 30.386
d_4 = 1.399	(C_{34} C_{36} C_{35}) = 30.881	d_4 = 1.402	(C_{36} C_{34} C_{38}) = 29.660
d_5 = 1.400	(C_{37} C_{41} C_{35}) = 29.240	d_5 = 1.403	(C_{40} C_{37} C_{38}) = 30.861
d_6 = 1.401	(C_{39} C_{41} C_{36}) = 30.881	d_6 = 1.392	(C_{35} C_{37} C_{34}) = 30.695
d_7 = 1.409		d_7 = 1.427	
d_8 = 1.016		d_8 = 1.023	
d_9 = 1.371		d_9 = 1.372	
d_{10} = 1.426		d_{10} = 1.424	
d_{11} = 1.097		d_{11} = 1.097	

Cl–PPA$_{HT}$		**Cl–PPA$_{HH}$**	
Interatomic Distances (Å)	**Angles (°)**	**Interatomic Distances (Å)**	**Angles (°)**
d_1 = 1.419	(N_{44} C_{39} C_{36}) = 116.773	d_1 = 1.446	(N_{48} $C_{35}$$C_{34}$) = 125.903
d_2 = 1.387	(C_{35} $O_{38}$$C_{43}$) = 120.253	d_2 = 1.412	(C_{38} $O_{43}$$C_{44}$) = 118.142
d_3 =1.441	(C_{36} C_{39} C_{34}) = 28.763	d_3 = 1.392	(C_{34} C_{35} C_{36}) = 30.563
d_4 = 1.415	(C_{34} C_{36} C_{35}) = 31.386	d_4 = 1.419	(C_{36} C_{34} C_{38}) = 29.012
d_5 = 1.383	(C_{37} C_{41} C_{35}) = 29.908	d_5 = 1.379	(C_{40} C_{37} C_{38}) = 30.869
d_6 = 1.425	(C_{39} C_{41} C_{36}) = 30.459	d_6 = 1.420	(C_{35} C_{37} C_{34}) = 31.088
d_7 = 1.367		d_7 = 1.382	
d_8 = 1.101		d_8 = 1.076	
d_9 = 1.335		d_9 = 1.362	
d_{10} = 1.445		d_{10} = 1.431	
d_{11} = 1.100		d_{11} = 1.096	

The doped forms of PPA reveal the influence of doping on the molecular structure related to the typical protonation process of polyaniline and its derivatives. The conduction mechanism of the salt–form of polyanilines (doped forms) allows the generation and disappearance of charged sites, while electroneutrality is maintained by mobile counter ions [126]. Indeed, the physicochemical properties of these macromolecules also depends on the counter ion of the Brønsted doping acid. Although counter ions are needed for the compensation of charge, their nature and size significantly influence on the electrical conductivity of conjugated polymers [7]. Finally, the results of interatomic distances and angle values show that both polymerization mechanisms (head–to–tail and head–to–head) are possible and depends on the synthesis parameters. In addition, structural characteristics were

maintained after polymerization, and the major influence on the molecular packing was performed by the counter ions in the doped polymers.

4.5. FTIR Analysis

The FTIR spectra of PPA have been analyzed by considering the correlation between the data obtained experimentally for $PPA1_{HT}$ and $PPA16_{HT\text{-}HH}$ and those calculated for PPA_{HT} and PPA_{HH}. **Fig. 19(a–d)** shows the experimental ($PPA1_{HT}$ and $PPA16_{HT\text{-}HH}$) and calculated (PPA_{HT} and PPA_{HH}) FTIR spectra, highlighting the main absorption bands.

The bands located from 2,905 cm^{-1} to 3,006 cm^{-1} (**Fig. 19b**) in the experimental spectra of $PPA1_{HT}$ and $PPA16_{HT\text{-}HH}$ are assigned to ν(N–H). Similar bands are identified from 3,515 cm^{-1} to 3,518 cm^{-1}, and from 3,427cm^{-1} to 3,514 cm^{-1} in the theoretical spectra of PPA_{HT} and PPA_{HH}, respectively. The aromatic $\nu(C–H)_{ring}$ bands are observed from 3,080 cm^{-1} to 3,138 cm^{-1}, and from 3,085 cm^{-1} to 3,159 cm^{-1} in the calculated spectra of PPA_{HT} and PPA_{HH}, respectively. A broad band assigned to $\nu(C–H)_{ring}$ is found at 2,836 cm^{-1} in the experimental spectra of $PPA1_{HT}$ and $PPA16_{HT\text{-}HH}$. Similar experimental results were previously reported [14].

The absorption bands located at 1,242 cm^{-1} (PPA_{HT}) and 1,249 cm^{-1} (PPA_{HH}) in the calculated spectra are related to $\nu(C–O–CH_3)$. Correlated absorption bands are found at 1,250 cm^{-1} in the experimental spectra of $PPA1_{HT}$ and $PPA16_{HT\text{-}HH}$.

The band located at 1,230 cm^{-1} in the calculated spectra of PPA_{HT} and PPA_{HH} is assigned to ν(C–O). This band is found at 1,173 cm^{-1} in the experimental spectra of $PPA1_{HT}$ and $PPA16_{HT\text{-}HH}$.

Bands related to $\nu(CH_3)$ are e observed in the experimental spectra of $PPA1_{HT}$ and $PPA16_{HT\text{-}HH}$ at 1,418 cm^{-1} [46]. These bands are found at 1,454 cm^{-1} in the calculated spectra.

The band related to the out-of-plane γ(C–H) in the aromatic rings is observed at 828 cm^{-1} in the $PPA1_{HT}$ and $PPA16_{HT\text{-}HH}$ spectra. Similar results were previously reported [127].

Correlated absorption bands are found in the theoretical spectra at 795 cm^{-1} and 774 cm^{-1}, respectively, for PPA_{HT} and PPA_{HH}.

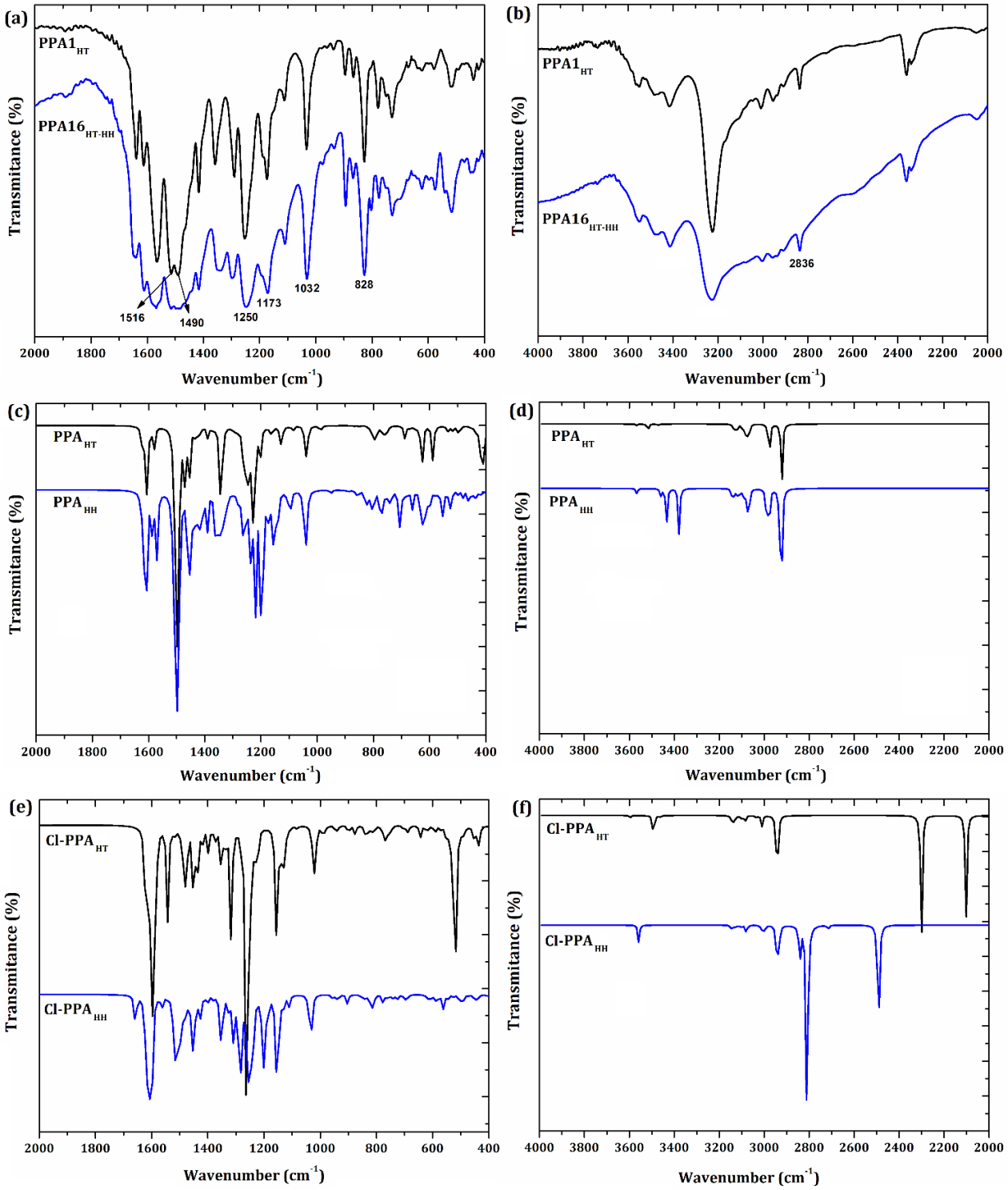

Figure 19. (a-b) Experimental FTIR spectra of $PPA1_{HT}$ and $PPA16_{HT-HH}$, (c-d) calculated FTIR spectra of PPA_{HT} and PPA_{HH} and (e-f) calculated spectra of $Cl–PPA_{HT}$ and $Cl–PPA_{HH}$.

The bands at 1,216 cm^{-1} and 1,228 cm^{-1} are found, respectively, in the calculated spectra of PPA_{HT} and PPA_{HH} due to ν(C–N–C). Correlated bands present a blueshift to 1,109 cm^{-1} in the experimental spectra probably as a consequence of the restrictions imposed by the coiled conformation of the bulk polymeric chains, as well as to the combination of HT and HH polymerization. Other absorption bands are observed due to $\nu(O–CH_3)$ at 1,039 cm^{-1} in the calculated spectra. Similar bands are verified in the experimental spectra at 1,032 cm^{-1}.

Bands observed in the experimental spectra of $PPA1_{HT}$ and $PPA16_{HT\text{-}HH}$ at 1,490 cm^{-1} and 1,516 cm^{-1} **[Fig. 19(a)]** are assigned to the quinoid (Q) and benzenoid (B) structures, respectively [14]. However, these bands appear to be less defined in the $PPA16_{HT\text{-}HH}$ spectrum. These absorption bands are related to the doping level of polyanilines and its derivatives [48]. The bands assigned to the benzenoid structure are found at 1,606 cm^{-1} in the theoretical spectra of PPA_{HT} and PPA_{HH}.

The Q and B structures present an important role in the oxidation states of polyaniline and its derivatives, and both structures comprise the emeraldine-salt form [128]. The ratio between band areas of the quinoid and benzenoid structures (Q/B) has been useful to estimate the doping level of polyaniline and its derivatives [129]. Significant modifications in the Q and B bands are observed in $PPA1_{HT}$ and $PPA16_{HT\text{-}HH}$ spectra. The Q/B value is found to be 1.0 for $PPA1_{HT}$ and 0.8 for $PPA16_{HT\text{-}HH}$, indicating decreased doping level in $PPA16_{HT\text{-}HH}$. Moreover, $PPA1_{HT}$ presents similar amount of Q and B structures, as expected in a half-oxidized emeraldine-salt form. This difference suggests that the Q structures are in smaller amount in the $PPA16_{HT\text{-}HH}$ polymer chains probably due to its lower degree of oxidation. This result may be correlated with the reagent concentration of $PPA16_{HT\text{-}HH}$ synthesis, influencing on the percentage of crystallinity, as well as on molecular structure conformation (combined HT and HH mechanisms of polymerization).

The structure and morphology of the hydrochloride polyaniline emeraldine-salt form (ES-PANI) synthesized by conventional and interfacial polymerization have been evaluated

based on different doping acid concentration [48]. The FTIR spectra are useful to evaluate significant changes in the Q and B bands: the conventional polymerization resulted in Q/B values from 0.4 to 0.6, indicating that the doping level increased for higher dopant acid concentration. An even more intense dopant effect was verified in the polymers resulted from interfacial polymerization, presenting Q/B values from 0.7 to 0.9. These results revealed the more efficient doping level as a result of the interfacial polymerization. The conventional and interfacial mechanisms of polymerization enhanced the percentage of crystallinity of polyaniline with different structures, suggesting that interfacial polymerization allowed better polymer chains alignment. **Table 4** shows the main experimental and calculated absorption bands from the FTIR spectra of PPA, also considering the doped molecular structures.

Table 3. Experimental and calculated absorption bands from the FTIR spectra of PPAHT, PPAHH, Cl–PPAHT, Cl–PPAHH, PPA1HT and PPA16HT-HH.

	Theoretical Absorptions				Experimental Absorptions	
Absorption bands	**PPA_{HT} (cm^{-1})**	**PPA_{HH} (cm^{-1})**	**Cl–PPA_{HT} (cm^{-1})**	**Cl–PPA_{HH} (cm^{-1})**	**$PPA1_{HT}$ (cm^{-1})**	**$PPA16_{HT\text{-}HH}$ (cm^{-1})**
γ(C–H)	795	774	763	759	828	828
ν(O–CH_3)	1,039	1,039	1,024	1,032	1,032	1,032
ν(C–N–C)	1,216	1,228	1,223	1,235	1,109	1,109
ν(C–O)	1,230	1,230	1,233	1,244	1,173	1,173
ν(C–O–CH_3)	1,242	1,249	1,253	1,257	1,250	1,250
ν(C=C)	1,337	1,339	1,336	1,324	1,358	1,344
ν(CH_3)	1,454	1,454	1,447	1,454	1,418	1,418
quinoid (Q)	–	–	1,537	1,513	1,490	1,490
benzenoid (B)	1,606	1,606	1,596	1,602	1,516	1,516
ν(C–H)$_{ring}$	3,080 – 3,138	3,085 – 3,159	3,090 – 3,156	3,101 – 3,153	2,836	2,836
ν(N–H)	3,515 – 3,518	3,427 – 3,514	2,101 and 2,300	2,491 – 2841	2,905 – 3,006	2,905 – 3,006

Fig. 19(e-f) shows the theoretical spectra of the Cl–PPA_{HT} and Cl–PPA_{HH} structures resulted from the doping process in the polymer chains. The spectra show the γ(C–H) absorption in the aromatic rings at 763 cm^{-1} and 759 cm^{-1}, respectively. The ν(O–CH_3) band is found at 1,024 cm^{-1} and 1,032 cm^{-1} for Cl–PPA_{HT} and Cl–PPA_{HH}, respectively. The ν(C–O–CH_3)

vibration is located at 1,253 cm^{-1} (Cl–PPA_{HT}) and 1,257 cm^{-1} (Cl–PPA_{HH}). The bands at 1,223 cm^{-1} and 1,235 cm^{-1} are assigned to ν(C–N–C) in the spectra of Cl–PPA_{HT} and Cl–PPA_{HH}, respectively.

The bands related to the Q structure is located at 1,537 cm^{-1} (Cl–PPA_{HT}) and 1,513 cm^{-1} (Cl–PPA_{HH}). The B structure is responsible for the absorption bands at 1,596 cm^{-1} (Cl–PPA_{HT}) and 1,602 cm^{-1} (Cl–PPA_{HH}).

The ν(N–H) bands observed in the calculated PPA_{HT} and PPA_{HH} present a significant blueshift in the spectra of the doped structures (Cl–PPA_{HT} and Cl–PPA_{HH}) due to the influence of the counter ions on the polymer chains. Additional intense bands are observed in the calculated spectra of Cl–PPA_{HT} at 2,101 cm^{-1} and 2,300 cm^{-1} [**Fig. 19(f)**] which are assigned to ν(N–H) influenced by the doping process. However, the ν(N–H) bands suffer blueshift (including additional bands) in the Cl–PPA_{HH} spectra from 2,491 cm^{-1} to 2,841 cm^{-1}. This is due to the electrostatic interaction between (H49) and counter ions during the doping process, as expected, influencing on the N–H bond length/stretching absorption.

Despite being influenced by the presence of counter ions, the HH and HT mechanisms of polymerization resulted in different molecular structures of PPA. In addition, the steric hindrance imposed by the head-to-head polymerization may also contribute to impair the N–H stretching. Moreover, the ν(N–H) bands are found in the range of 2,905 cm^{-1} – 3,006 cm^{-1} in both experimental spectra of $PPA1_{HT}$ and $PPA16_{HT\text{-}HH}$ due to the same reasons described above, and also probably due to the larger concentration of head-to-tail polymerization in $PPA16_{HT\text{-}HH}$ [as observed from the ^{13}C NMR results, (62.0 ± 0.5) %].

In general, the main changes in the calculated spectra show the influence of counter ions on the molecular structure, especially on the ν(N–H) absorption. On the other hand, the experimental spectra did not show significant differences in $PPA1_{HT}$ and $PPA16_{HT\text{-}HH}$ probably due to the predominance of the head-to-tail polymerization in both structures. Comparing calculated and experimental spectra, the most pronounced changes have been observed in ν(C–

H), ν(N–H), ν(C–O) and ν(C–N–C), caused by the doping process, as well as by the different mechanisms of polymer conformation.

4.6. Electrical Conductivity

The degree of protonation and the conductivity have been found in a wide range in PANI and its derivatives mainly due to differences in conformation of the polymer chains and packing [13]. While the structure of the π-conjugated backbone is responsible for imparting the core optoelectronic and electrochemical functionality of the polymer, side chains appended to the backbone play an important role in tuning these properties [130].

The mechanisms of charge conduction are still not completely understood mainly due to the diversity of factors affecting conductivity along the polymer chains in PANI and its derivatives. More specifically, side chains may influence the doping mechanism and efficiency, long-range order and polymer packing, and morphology of conjugated polymers [13].

Analyses based on a combination of techniques including *dc* conductivity measurements can provide useful information on the nature of charge localization. The electrical conductivity of most PANI-based materials is found to show a temperature dependence [131]. **Fig. 20(a)** represents the equivalent circuit used to adjust the polymers $PPA1_{HT}$ and $PPA16_{HT\text{-}HH}$, where R_1 and R_2 correspond to the resistance of the most crystalline region (considered here as conducting islands) and the region of lower crystallinity, respectively. The capacitance and the phase constant element are represented by C_1 and CPE_1, respectively. The values of CPE_1 close to 1 correspond to a more capacitive character, while values around 0.5 are associated to a more resistive material.

In **Fig. 20(b)** the Cole-Cole diagrams and their respective adjustments for $PPA1_{HT}$ and $PPA16_{HT\text{-}HH}$ are observed. In this case, the semicircle with larger diameter (higher strength) corresponds to $PPA16_{HT\text{-}HH}$, which possesses lower crystallinity as previously revealed by the

XRD results. From the results obtained by equivalent circuit, the total resistance ($R_t = R_1 + R_2$) of this polymer was found around 10^{10} Ω. Reduced crystallinity may have negatively influenced the mobility of the charge carriers due to the lack of conducting paths/islands allowing the long-range mobility. Finally, total resistance of PPA1$_{HT}$ (which shows the highest crystallinity) was found to be of the order of 10^7 Ω. **Fig. 20(c)** shows a better visualization of the Cole-Cole diagram for PPA1$_{HT}$. **Table 5** shows the R_t and polymer resistivity (ρ = R_t x S/d) values, where *S* and *d* are, the area and thickness of the pellets, respectively.

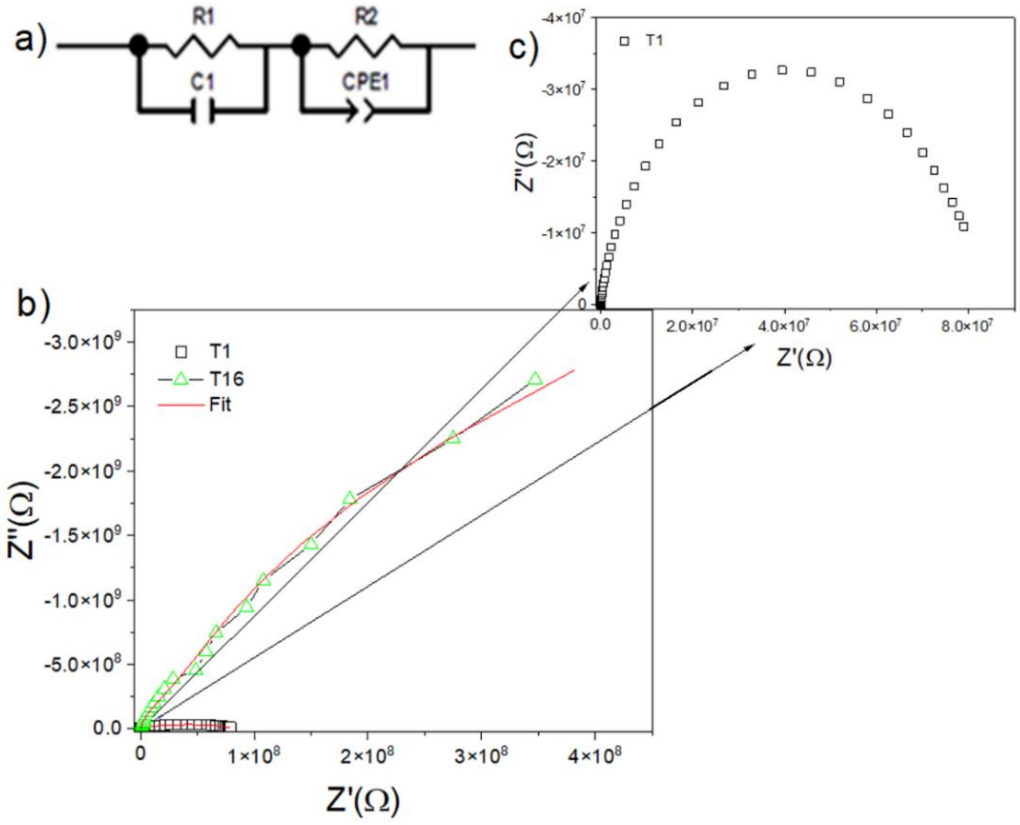

Figura 20. (a) Equivalent circuit used for sample adjustment, (b) Cole-Cole diagram with symbols for the different polymers and (c) enlargement of the Cole-Cole diagram of the PPA1$_{HT}$ polymer.

The capacitance values are similar and of the same order of magnitude in PPA1$_{HT}$ and PPA16$_{HT\text{-}HH}$. However, a significant difference in resistivity values was observed in the range of 8.23 x10^2 MΩcm and 2.56 x 10^7 MΩcm, respectively, for PPA1$_{HT}$ and PPA16$_{HT\text{-}HH}$. Considering

the extreme points, $PPA1_{HT}$ (maximum crystallinity) and $PPA16_{HT\text{-}HH}$ (minimum crystallinity), a difference of resistivity of 5 orders of magnitude was observed.

Table 4. Tuning parameters using the equivalent circuit model (R1, R2, C1, CPE). Rt and ρ parameters were calculated from the adjusting results.

Sample	R_1(MΩ)	R_2(MΩ)	R_t(MΩ)	C_1(μF)	$C_{PE1\text{-}T}$	$C_{PE1\text{-}T}$	ρ(MΩcm)	σ(S.cm^{-1})
$PPA1_{HT}$	3.34	77.31	80.65	6.96 x 10^{-5}	3.60 x 10^{-5}	0.90	8.23 x10^{2}	1.00 x 10^{-9}
$PPA16_{HT\text{-}HH}$	30.9	2.89 x 10^{4}	289.9 x 10^{4}	5.65 x 10^{-5}	6.09 x 10^{-5}	0.98	2.56 x 10^{7}	3.90 x 10^{-14}

It is widely accepted that the doped molecules of PANI and its derivatives are not uniformly distributed, but rather agglomerated into conducting islands [13]. Furthermore, as structural disorder is associated to the localization of charges within the polymer matrix, this leads to the development of electronic traps, which limits the charge transfer, a phenomenon known as charge transfer hindrance [132]. Most conducting polymers show irregular channels, with the small islands immersed in a less dense, insulating matrix. Previous report pointed to the increased number of conducting islands as a function of the degree of doping in POEA [13].

Our results indicate that the resistivity values of $PPA1_{HT}$ and $PPA16_{HT\text{-}HH}$ are closely related to the amount of conducting crystallites in a non-crystalline matrix. It is not known whether the morphologies previously observed in the SEM images are purely related to the crystalline (needles) and non-crystalline (globules) phases. Previous report on POMA [10] evaluated the morphology of the doping form constituted entirely of vesicular globules presenting considerable degree of crystallinity as a function of the time of synthesis. For this reason, the globules, better observed in $PPA16_{HT\text{-}HH}$, may also present semi crystalline structure.

What can be stated here is that the synthesis conditions resulted in polymers with different structural characteristics and different levels of doping, directly influenced the resistivity values. The chains in the crystalline regions (more pronounced in $PPA1_{HT}$) should be

better aligned, which would increase electron delocalization. There is a finite density of states of conduction electrons around the Fermi levels in doped conjugated polymers, and the carriers may be spatially localized due to the structural disorder [54]. In the case of PPA16$_{HT-HH}$, the homogeneously disordered regions limit the overlapping of wave functions [42]. In this case, conduction can only take place through hopping [13,133]. This result may be a consequence of the non-existence of efficient conducting paths allowing the long-range mobility of charge carriers. The resistivity values obtained in this work , as reported in Table 7, are similar to those previously reported [134].

A wide range of electrical conductivity values have been found in scientific literature for *ortho*, *meta* and *para*-substituted polyanilines. Emeraldine-salt form of POMA was chemically synthesized with time of synthesis ranging from 0.5 to 72 h [10]. The authors observed that the percentage of crystallinity increased as a function of time, and the polymer obtained at 72 h presented the highest value of electrical conductivity. Interestingly, the more conducting, crystalline POMA presented undefined morphology, showing a loss of globular morphology when the time of synthesis was increased. Electrical conductivity of POMA was found as 5.18 x 10^{-7} S/cm (0.5 h of synthesis, 48 % crystallinity) to 8.89 x 10^{-7} S/cm (72 h of synthesis, 63 % crystallinity).

The electrical conductivity of poly(*m*-anisidine) (PMA), as a function of frequency and different dopant acids, was obtained to be 3.32 x 10^{-7} S/cm, 5.16 x 10^{-9} S/cm and 4.95 x 10^{-10} S/cm for PMA/H_2SO_4, PMA/HNO_3 and PMA/HCl, respectively [7]. These values are similar to those previously calculated from the total resistance. The nature of the doping acid and counterion size significantly influenced on the charge mobility in conjugated polymers. However, the authors observed that the PMA doped with HCl surprisingly presented reduced electrical conductivity. Theoretical evaluation via DFT was performed, and a charge transfer was verified between polymer chains and counterions. The polymer PMA/HCl presented the

HOMO band partially filled, while in PMA/H_2SO_4 a fully occupied band was verified, resulting in a near-zero gap semiconductor behavior.

There is, however, a lack of consistent data on electrical conductivity of PPA. Moreover, the few published results that are available in the literature vary over a wide range values, making it difficult to find a correlation among them. Composites formed by PPA and MnO_2 were prepared in different concentrations via oxidative polymerization using HCl as dopant acid and KIO_3 as oxidizing agent [135]. The authors reported the electrical conductivity of the pure PPA in the range of 5.9 x 10^{-4} S/cm, and the composites PPA/MnO_2 presented reduced electrical conductivity when the percentage of MnO_2 was increased from 8.6 x 10^{-3} S/cm (13 % of MnO_2) to 5.2 x 10^{-3} S/cm (52 % MnO_2). Another published study proposed the preparation of nanocomposites synthesized by oxidative polymerization of *p*-anisidine and/or aniline monomers with TiO_2 nanoparticles in the presence of hydrochloric acid and ammonium persulfate. The electrical conductivity values of nanocomposites were found in the range of 0.08 – 0.91 S/cm, following the tendency of the pure polymers [46]. The composite based on PANI and PPA presented, respectively, the higher and lower electrical conductivity values. The pure PPA presented electrical conductivity in the range of 0.22 S/cm.

5. CONCLUSIONS

Poly(*p*–anisidine) was successfully synthesized based on different concentrations of monomer, dopant acid and oxidizing agent, resulting on polymers with different percentage of crystallinity. Their structural, morphological, spectroscopic and electrical properties were found to be significantly related to the nature of the monomer polymerization.

The major challenge of this research was to understand and propose a bonding mechanism of the *p*–anisidine monomers to form the PPA polymer chains. The ^{13}C NMR analysis allowed the proposition of the polymerization mechanisms, revealing that $PPA1_{HT}$ was purely

formed by head-to-tail (HT) polymerization, while $PPA16_{HT\text{-}HH}$ was formed by two different molecular arrangements composed of head-to-tail (HT) and head-to-head (HH) polymerization. The scientific literature was not clear about the fashion in which the *p*–anisidine monomers form the polymeric structure. Then, the HT and HH mechanisms of polymerization resulted in different crystal structures and morphologies, which were correlated to explain the SEM images and XRD patterns. Basically, the needle-like morphology was mainly resulted from the HT polymerization, while a mixture of needles and globules essentially formed the morphology of the combined HT-HH polymerization.

Most of experimental results were supported by theoretical analysis via DFT, confirming the fashion (*modus operandi*) in which the polymer chains were formed in both PPA. These results were significantly important for spectroscopic evaluation, allowing the confirmation of the main vibrational stretching modes in both HT and HH polymers. The calculated spectra pointed to the influence of counter ions on the molecular structure, especially on the ν(N–H) absorption. On the other hand, the experimental spectra did not show significant differences in $PPA1_{HT}$ and $PPA16_{HT\text{-}HH}$ probably due to the predominance of the head-to-tail polymerization in both structures. Finally, the electrical conductivity results revealed the resistive behavior of the as-synthesized PPA.

All results proposed herein on PPA are considerably important for the scientific community due to the lack of information on *para*–substituted polyanilines. We hope this present research can stimulate further studies on PPA, since other information (such as thermal and optical properties) is still necessary. Due to the important role of conjugated polymers in novel technological applications, we highlighted here the importance of combined experimental and theoretical results for better understanding of the experimental results. Finally, the possibilities of research on PANI, POMA, PMA and PPA continue to be extremely broad, promising and capable of competing directly with other semiconducting materials.

SPECIAL ACKNOWLEDGMENTS

The authors thank CAPES (Coordenação de Aperfeiçoamento de Pessoal de Nível Superior – Código Financeiro 001), CNPq (Conselho Nacional de Desenvolvimento Científico e Tecnológico, FAPEAM [Fundação de Amparo à Pesquisa do Estado do Amazonas, RESOLUÇÃO N. 002/2018 - POSGRAD 2018 – UFAM (Processo 062.00478/2019 – Lilian Rodrigues de Oliveira) for the financial support, as well as the Laboratório de Microscopia Eletrônica (CDMF - Centro de Desenvolvimento de Materiais Funcionais) – Federal University of São Carlos (UFSCar).

REFERENCES

1. Koval'chuk, E.P.; Stratan, N. V; Reshetnyak, O. V; Blaejowski, J.; Whittingham, M.S. Synthesis and properties of the polyanisidines. In Proceedings of the Solid State Ionics; 2001; Vol. 141–142, pp. 217–224.
2. Pron, A.; Rannou, P. Processible conjugated polymers: from organic semiconductors to organic metals and superconductors. *Prog. Polym. Sci.* **2002**, *27*, 135–190, doi:10.1016/S0079-6700(01)00043-0.
3. Orlov, A. V.; Kiseleva, S.G.; Karpacheva, G.P.; Muratov, D.G. Peculiarities of oxidative polymerization of diarylaminodichlorobenzoquinones. *Polymers (Basel).* **2021**, *13*, 3657, doi:10.3390/polym13213657.
4. Sanches, E.A.; Soares, J.C.; Mafud, A.C.; Fernandes, E.G.R.; Leite, F.L.; Mascarenhas, Y.P. Structural characterization of chloride salt of conducting polyaniline obtained by XRD, SAXD, SAXS and SEM. *J. Mol. Struct.* **2013**, *1036*, 121–126, doi:10.1016/j.molstruc.2012.09.084.
5. Sapurina, I.Y.; Stejskal, J. Oxidation of aniline with strong and weak oxidants. *Russ. J. Gen. Chem.* **2012**, *82*, 256–275, doi:10.1134/S1070363212020168.
6. Angaleeswari, B.; Dura Amirtham, R.M.; Jeevithaa, T.; Vaishnavi, V.; Eevera, T.; Berchmans, S.; Yegnaraman, V. Poly(o-anisidine)-anion composite films as sensing platform for biological molecules. *Sensors Actuators, B Chem.* **2008**, *129*, 558–565, doi:10.1016/j.snb.2007.09.003.
7. Veras, T.N.; Carolino, A.S.; Lima, S.X.; Biondo, M.M.; Santos, N.A.; Campelo, P.H.; Ruiz, Y.L.; Frota, H.O.; Sanches, E.A. Characterization and DFT calculation of poly(m-anisidine) synthesized with different dopant acids. *J. Mol. Struct.* **2020**, *1201*, 127182, doi:10.1016/j.molstruc.2019.127182.

8. Biondo, M.M.; Medeiros de Oliveira, L.; Lima, S.X.; Carolino, A.D.S.; Farias Rocha, A.L.; da Silva, J.P.; Ruiz, Y.L.; Giacon, V.M.; Campelo, P.H.; Sanches, E.A. Chemically synthesized poly(o-methoxyaniline): Influence of counterions on the structural and electrical properties. *J. Mol. Struct.* **2020**, *1205*, doi:10.1016/j.molstruc.2019.127588.

9. Biondo, M.M.; Medeiros de Oliveira, L.; Lima, S.X.; Carolino, A. de S.; Farias Rocha, A.L.; da Silva, J.P.; Ruiz, Y.L.; Giacon, V.M.; Campelo, P.H.; Sanches, E.A. Chemically synthesized poly(o-methoxyaniline): Influence of counterions on the structural and electrical properties. *J. Mol. Struct.* **2020**, *1205*, 127588, doi:10.1016/j.molstruc.2019.127588.

10. Sanches, E.A.; Soares, J.C.; Mafud, A.C.; Trovati, G.; Fernandes, E.G.; Mascarenhas, Y.P. Structural and morphological characterization of chloride salt of conducting poly(o-methoxyaniline) obtained at different time synthesis. *J. Mol. Struct.* **2013**, *1039*, 167–173, doi:10.1016/j.molstruc.2012.12.025.

11. Sanches, E.A.; Gomes, L.C.A.; Soares, J.C.; Da Silva, G.R.; Mascarenhas, Y.P. Characterization of Poly(o-methoxyaniline) Emeraldine-base form obtained at different time neutralization. *J. Mol. Struct.* **2014**, *1063*, 336–340, doi:10.1016/j.molstruc.2014.01.082.

12. Silva, A.D.S.; Soares, J.C.; Mafud, A.C.; De Souza, S.M.; Fernandes, E.G.R.; Mascarenhas, Y.P.; Sanches, E.A. Structural and morphological characterization of Poly(o-ethoxyaniline) Emeraldine-salt form using FTIR, XRD, Le Bail Method and SEM. *J. Mol. Struct.* **2014**, *1071*, 1–5, doi:10.1016/j.molstruc.2014.04.039.

13. Leite, F.L.; Alves, W.F.; Mir, M.; Mascarenhas, Y.P.; Herrmann, P.S.P.; Mattoso, L.H.C.; Oliveira, O.N. TEM, XRD and AFM study of poly(o-ethoxyaniline) films: New evidence for the formation of conducting islands. *Appl. Phys. A Mater. Sci. Process.* **2008**, *93*, 537–542, doi:10.1007/s00339-008-4686-9.

14. K, R.; N, V.; D, T. Electrical conductivity study of poly(p-anisidine) doped and undoped ZnO nanocomposite. *Mediterr. J. Chem.* **2019**, *9*, 403–410, doi:10.13171/mjc01912071050kr.

15. Morales, G.M.; Llusa, M.; Miras, M.C.; Barbero, C. Effects of high hydrochloric acid concentration on aniline chemical polymerization. *Polymer (Guildf).* **1997**, *38*, 5247–5250, doi:10.1016/S0032-3861(97)82751-6.

16. Gazotti Junior, W.A. Preparação e caracterização da poli(o-metoxianilina) dopada como ácidos funcionalizados e sua utilização em aplicações de interesse tecnológico 1998, 166.

17. Komsiyska, L.; Tsacheva, T.; Tsakova, V. Electrochemical formation and copper modification of poly-o-methoxyaniline. *Thin Solid Films* **2005**, *493*, 88–95, doi:10.1016/j.tsf.2005.07.265.

18. Leite, F.L.; Alves, W.F.; Neto, M.O.; Polikarpov, I.; Herrmann, P.S.P.; Mattoso, L.H.C.; Oliveira, O.N. Doping in poly(o-ethoxyaniline) nanostructured films studied with atomic force spectroscopy (AFS). *Micron* **2008**, *39*, 1119–1125, doi:10.1016/j.micron.2008.07.003.

19. Zare, E.N.; Motahari, A.; Sillanpää, M. Nanoadsorbents based on conducting polymer nanocomposites with main focus on polyaniline and its derivatives for removal of heavy metal ions/dyes: A review. *Environ. Res.* **2018**, *162*, 173–195, doi:10.1016/j.envres.2017.12.025.

20. Dong, Y.Z.; Kim, H.M.; Choi, H.J. Conducting polymer-based electro-responsive smart suspensions. *Chem. Pap.* **2021**, *75*, 5009–5034, doi:10.1007/s11696-021-01550-w.

21. Dong, Y.Z.; Choi, K.; Kwon, S.H.; Nam, J.-D.; Choi, H.J. Nanoparticles functionalized by conductingpolymers and their electrorheological and magnetorheological applications. *Polymers (Basel).* **2020**, *12*, 204, doi:10.3390/polym12010204.

22. Cheng, M.; Meng, Y.; Wei, Z. Conducting polymer nanostructures and their derivatives for flexible supercapacitors. *Isr. J. Chem.* **2018**, *58*, 1299–1314, doi:10.1002/ijch.201800077.

23. Ma, G.; Zhao, S.; Wang, Y.; Wang, Z.; Wang, J. Conjugated polyaniline derivative membranes enable ultrafast nanofiltration and organic-solvent nanofiltration. *J. Memb. Sci.* **2022**, *645*, 120241, doi:10.1016/j.memsci.2021.120241.

24. Zeng, M.; Zhu, W.; Luo, J.; Song, N.; Li, Y.; Chen, Z.; Zhang, Y.; Wang, Z.; Liang, W.; Guo, B.; et al. Highly efficient nonfullerene organic solar cells with a self-doped water-soluble neutral polyaniline as hole transport layer. *Sol. RRL* **2021**, *5*, 2000625, doi:10.1002/solr.202000625.

25. Guo, B.; Ma, P.X. Conducting polymers for tissue engineering. *Biomacromolecules* **2018**, *19*, 1764–1782, doi:10.1021/acs.biomac.8b00276.

26. Armes, S.P.; Miller, J.F. Optimum reaction conditions for the polymerization of aniline in aqueous solution by ammonium persulphate. *Synth. Met.* **1988**, *22*, 385–393, doi:10.1016/0379-6779(88)90109-9.

27. Gonçalves, D.; dos Santos, D.S.; Mattoso, L.H.C.; Karasz, F.E.; Akcelrud, L.; Faria, R.M. Poly (o-methoxy aniline): solubility, deprotonation-protonation process in solution and cast films. *Synth. Met.* **1997**, *90*, 5–11, doi:10.1016/S0379-6779(97)03895-2.

28. Kim, S.C.; Huh, P.; Kumar, J.; Kim, B.; Lee, J.O.; Bruno, F.F.; Samuelson, L.A. Synthesis of polyaniline derivatives via biocatalysis. *Green Chem.* **2007**, *9*, 44–48, doi:10.1039/b606839a.

29. Bavastrello, V.; Correia Terencio, T.B.; Nicolini, C. Synthesis and characterization of polyaniline derivatives and related carbon nanotubes nanocomposites - Study of optical properties and band gap calculation. *Polymer (Guildf).* **2011**, *52*, 46–54, doi:10.1016/j.polymer.2010.10.022.

30. Sayyah, S.M.; El-Rabiey, M.M.; El-Feky, H.; Gaber, A.F. Electropolymerization of 2-methoxyaniline: Kinetic studies, mechanism, characterization of the polymer and applications as corrosion protection for mild steel in acid medium. *Int. J. Polym. Mater. Polym. Biomater.* **2007**, *56*, 605–628, doi:10.1080/00914030600992285.

31. Bardakçi, B.; Kaya, N.; Kalayci, T. Anisidine adsorption on Co-supported pumice. *Environ. Earth Sci.* **2012**, *70*, 849–856, doi:10.1007/s12665-012-2173-2.

32. Koval'chuck, E.P.; Stratan, V.N.; Reshentnyak, V.O.; J., B.; M., W.S. Synthesis and Properties of the Polyanisidines. *Solid State Ionics* **2001**, 217–224, doi:10.1021/ar300348n.(2).

33. Sayyah, S.M.; Kamal, S.M.; El-rehim, S.S.A.; Ibrahim, M.A.; Branch, B. Electrochemical Polymerization of 3-Methoxyaniline and Characterization of the Obtained Polymer. *Int. J. Polym. Mater. Polym. Biomater.* **2006**, 339–357.

34. Profeti, D.; Profeti, L.P.R.; Olivi, P. Effects of electrochemical synthesis conditions on

poly(o-methoxyaniline) thin films formation. *Mater. Chem. Phys.* **2018**, *213*, 96–101, doi:10.1016/j.matchemphys.2018.03.075.

35. Tsai, C.H.; Huang, W.C.; Hsu, Y.C.; Shih, C.J.; Teng, I.J.; Yu, Y.H. Poly(o-methoxyaniline) doped with an organic acid as cost-efficient counter electrodes for dye-sensitized solar cells. *Electrochim. Acta* **2016**, *213*, 791–801, doi:10.1016/j.electacta.2016.08.012.

36. Alves, W.F.; Venancio, E.C.; Leite, F.L.; Kanda, D.H.F.; Malmonge, L.F.; Malmonge, J.A.; Mattoso, L.H.C. Thermo-analyses of polyaniline and its derivatives. *Thermochim. Acta* **2010**, *502*, 43–46, doi:10.1016/j.tca.2010.02.003.

37. Chaudhari, S.; Patil, P.P. Corrosion protective poly(o-ethoxyaniline) coatings on copper. *Electrochim. Acta* **2007**, *53*, 927–933, doi:10.1016/j.electacta.2007.08.002.

38. Behbahani, M.; Bide, Y.; Salarian, M.; Niknezhad, M.; Bagheri, S. The use of tetragonal star-like polyaniline nanostructures for efficient solid phase extraction and trace detection of Pb (II) and Cu (II) in agricultural products , sea foods , and water samples. *Food Chem.* **2014**, *158*, 14–19, doi:10.1016/j.foodchem.2014.02.110.

39. Jamal, S.; Rezaei, T.; Bide, Y.; Nabid, M.R. A new approach for the synthesis of polyaniline microstructures with a unique tetragonal star-like morphology. *Synth. Met.* **2011**, *161*, 1414–1419, doi:10.1016/j.synthmet.2011.05.011.

40. Maggi, R.; Schlosser, M. Optional Site Selectivity in the Metalation of o - and p -Anisidine through Matching of Reagents with Neighboring Groups. **1996**, *3263*, 5430–5434.

41. Macdiarmid, A.G. Synthetic Metals: A Novel Role for Organic Polymers (Nobel Lecture). *Chem. Int Ed.* **2001**, *40*, doi:1433-7851/01/4014-2581.

42. Luo, C.; Peng, H.; Zhang, L.; Lu, G.-L.; Wang, Y.; Travas-Sejdic, J. Formation of nano-/microstructures of polyaniline and its derivatives. *Macromolecules* **2011**, *44*, 6899–6907, doi:10.1021/ma201350m.

43. Sharma, R.; Dave, S. Electrochemical Studies of o- and p- anisidine. *Int. J. Appl. Sci. Biotchenology* **2015**, *3*, 267–271, doi:10.3126/ijasbt.v3i2.12615.

44. Bhat, I.; Chaithanya, S.; Satyanarayana, P.D.; Kalluraya, B. The synthesis and antimicrobial study of some azetidinone derivatives with the para-anisidine moiety. *J. Serbian Chem. Soc.* **2007**, *72*, 437–442, doi:10.2298/JSC0705437B.

45. Kumar Trivedi, M. Physicochemical Characterization of Biofield Energy Treated Calcium Carbonate Powder. *Am. J. Heal. Res.* **2015**, *3*, 368, doi:10.11648/j.ajhr.20150306.19.

46. Chouli, F.; Radja, I.; Morallon, E.; Benyoucef, A. A novel conducting nanocomposite obtained by p-anisidine and aniline with titanium(IV) oxide nanoparticles: Synthesis, Characterization, and Electrochemical properties. *Polym. Compos.* **2017**, *38*, E254–E260, doi:10.1002/pc.23837.

47. Shishov, M.; Moshnikov, V.; Sapurina, I. Self-organization of polyaniline during oxidative polymerization: formation of granular structure. *Chem. Pap.* **2013**, *67*, doi:10.2478/s11696-012-0284-6.

48. Ferreira, A.A.; Sanches, E.A. Multimorphologies of hydrochloride polyaniline synthesized by conventional and interfacial polymerization. *J. Mol. Struct.* **2017**, *1143*, 294–305, doi:10.1016/j.molstruc.2017.04.104.

49. Dong, B.X.; Wenderott, J.K.; Green, P.F. Charge carrier transport in thin conjugated

polymer films: influence of morphology and polymer/substrate interactions. *Colloid Polym. Sci.* **2021**, *299*, 439–456, doi:10.1007/s00396-020-04725-1.

50. Fan, B.; Li, M.; Zhang, D.; Zhong, W.; Ying, L.; Zeng, Z.; An, K.; Huang, Z.; Shi, L.; Bazan, G.C.; et al. Tailoring regioisomeric structures of π-conjugated polymers containing monofluorinated π-bridges for highly efficient polymer solar cells. *ACS Energy Lett.* **2020**, *5*, 2087–2094, doi:10.1021/acsenergylett.0c00939.

51. Hosseini, H.; Zirakjou, A.; Goodarzi, V.; Mousavi, S.M.; Khonakdar, H.A.; Zamanlui, S. Lightweight aerogels based on bacterial cellulose/silver nanoparticles/polyaniline with tuning morphology of polyaniline and application in soft tissue engineering. *Int. J. Biol. Macromol.* **2020**, *152*, 57–67, doi:10.1016/j.ijbiomac.2020.02.095.

52. Wegner, G.; Fischer, E.W.; Muñoz-Escalona, A. Crystal structure and morphology of polymers from solid-state reactions. *Die Makromol. Chemie* **1975**, *1*, 521–558, doi:10.1002/macp.1975.020011975136.

53. Veras, T.N.; Carolino, A.S.; Lima, S.X.; Biondo, M.M.; Santos, N.A.; Campelo, P.H.; Ruiz, Y.L.; Frota, H.O.; Sanches, E.A. Characterization and DFT calculation of poly(m-anisidine) synthesized with different dopant acids. *J. Mol. Struct.* **2020**, *1201*, doi:10.1016/j.molstruc.2019.127182.

54. da Silva, J.M.S.; de Souza Carolino, A.; de Oliveira, L.R.; de Souza Gonçalves, D.; Biondo, M.M.; Campelo, P.H.; de Araújo Bezerra, J.; Ţălu, Ş.; da Fonseca Filho, H.D.; da Frota, H.O.; et al. Poly(o-methoxyaniline) chain degradation based on a heat treatment (HT) process: Combined experimental and theoretical evaluation. *Molecules* **2022**, *27*, 3693, doi:10.3390/molecules27123693.

55. Bhandari, S. Polyaniline. In *Polyaniline Blends, Composites, and Nanocomposites*; Elsevier, 2018; pp. 23–60.

56. Sanches, E.A.; Soares, J.C.; Iost, R.M.; Marangoni, V.S.; Trovati, G.; Batista, T.; Mafud, A.C.; Zucolotto, V.; Mascarenhas, Y.P. Structural characterization of emeraldine-salt polyaniline/gold nanoparticles complexes. *J. Nanomater.* **2011**, *2011*, 1–7, doi:10.1155/2011/697071.

57. Bhadra, S.; Khastgir, D. Determination of crystal structure of polyaniline and substituted polyanilines through powder X-ray diffraction analysis. *Polym. Test.* **2008**, *27*, 851–857, doi:10.1016/j.polymertesting.2008.07.002.

58. de Oliveira, L.R.; Manzato, L.; Mascarenhas, Y.P.; Sanches, E.A. The influence of heat treatment on the semi-crystalline structure of polyaniline Emeraldine-salt form. *J. Mol. Struct.* **2017**, *1128*, 707–717, doi:10.1016/j.molstruc.2016.09.044.

59. Andriianova, A.N.; Biglova, Y.N.; Mustafin, A.G. Effect of structural factors on the physicochemical properties of functionalized polyanilines. *RSC Adv.* **2020**, *10*, 7468–7491, doi:10.1039/C9RA08644G.

60. MacDiarmid, A.G. Polyaniline and polypyrrole: Where are we headed? *Synth. Met.* **1997**, *84*, 27–34, doi:10.1016/S0379-6779(97)80658-3.

61. Babel, V.; Hiran, B.L. A review on polyaniline composites: Synthesis, characterization, and applications. *Polym. Compos.* **2021**, *42*, 3142–3157, doi:10.1002/pc.26048.

62. Liao, G.; Li, Q.; Xu, Z. The chemical modification of polyaniline with enhanced properties: A review. *Prog. Org. Coatings* **2019**, *126*, 35–43, doi:10.1016/j.porgcoat.2018.10.018.

63. Poddar, A.K.; Patel, S.S.; Patel, H.D. Synthesis, characterization and applications of conductive polymers: A brief review. *Polym. Adv. Technol.* **2021**, *32*, 4616–4641, doi:10.1002/pat.5483.

64. Banerji, A.; Tausch, M.W.; Scherf, U. Classroom Experiments and Teaching Materials on OLEDs with Semiconducting Polymers. *Educ. Química* **2013**, *24*, 17–22, doi:10.1016/s0187-893x(13)73190-2.

65. Heeger, A.J. Semiconducting and Metallic Polymers: The Fourth Generation of Polymeric Materials (Nobel Lecture) Copyright(c) The Nobel Foundation 2001. We thank the Nobel Foundation, Stockholm, for permission to print this lecture. *Angew. Chem. Int. Ed. Engl.* **2001**, *40*, 2591–2611, doi:10.1002/1521-3773(20010716)40:14<2591::AID-ANIE2591>3.0.CO.

66. Kar, P. *Doping in Conjugated Polymers*; Wiley; ISBN 9781118573808.

67. Andreu, Y.; De Marcos, S.; Castillo, J.R.; Galbán, J. Sensor film for Vitamin C determination based on absorption properties of polyaniline. *Talanta* **2005**, *65*, 1045–1051, doi:10.1016/j.talanta.2004.08.036.

68. Faez, R.; Reis, C.; Freitas, P.S. de; Kosima, O.K.; Ruggeri, G.; Paoli, M.-A. de Polímeros Condutores. *Química Nov. na Esc.* **2000**, *11*, 13–18, doi:10.1017/CBO9781107415324.004.

69. Dias, I.F.L.; Silva, M.A.T. *Polímero Semicondutores*; Livraria da Física, 2012;

70. Kaner, R.B.; MacDiarmid, A.G. Plastics That Conduct Electricity. *Sci. Am.* **1988**, *258*, 106–111, doi:10.1038/scientificamerican0288-106.

71. BORGES, F.S. *Elementos de cristalografia*; 2nd ed.; Fundação Lacouste Gulbenkian.: Lisboa, 1980;

72. D'Aprano, G.; Leclerc, M.; Zotti, G.; Schiavon, G. Synthesis and Characterization of Polyaniline Derivatives: Poly(2-alkoxyanilines) and Poly(2,5-dialkoxyanilines). *Chem. Mater.* **1995**, *7*, 33–42, doi:10.1021/cm00049a008.

73. Lindfors, T.; Ivaska, A. pH sensitivity of polyaniline and its substituted derivatives. *J. Electroanal. Chem.* **2002**, *531*, 43–52, doi:10.1016/S0022-0728(02)01005-7.

74. Mohanty, J.; Behera, P.; Mishra, R.S.; Badapanda, T.; Anwar, S. Dielectric and conduction behaviour of H2SO4 doped conducting Polyaniline. *J. Phys. Conf. Ser.* **2017**, *755*, doi:10.1088/1742-6596/755/1/011001.

75. Sanjai, B.; Raghunathan, A.; Natarajan, T.S.; Rangarajan, G. Charge transport and magnetic properties in polyaniline doped with methane sulphonic acid and polyaniline-polyurethane blend. *Phys. Rev. B* **1997**, *55*, 10734–10744, doi:10.1103/PhysRevB.55.10734.

76. Babu, V.J.; Vempati, S.; Ramakrishna, S. Conducting Polyaniline-Electrical Charge Transportation. *Mater. Sci. Appl.* **2013**, *04*, 1–10, doi:10.4236/msa.2013.41001.

77. Pizzi, G.; Volja, D.; Kozinsky, B.; Fornari, M.; Marzari, N. An updated version of BOLTZWANN: A code for the evaluation of thermoelectric and electronic transport properties with a maximally-localized Wannier functions basis. *Comput. Phys. Commun.* **2014**, *185*, 2311–2312, doi:10.1016/j.cpc.2014.05.004.

78. Kang, S.D. Charge-transport model for conducting polymers. **2016**, *1*, 1–7,

doi:10.1038/NMAT4784.

79. Prigodin, V.N.; Pstein, A.J. Charge Transport in Conducting Polymers. In *Introduction to Organic Electronic and Optoelectronic Materials and Devices*; CRC Press, 2017; pp. 101–141.

80. Leite, F.L.; Alves, W.F.; Mir, M.; Mascarenhas, Y.P.; Herrmann, P.S.P.; Mattoso, L.H.C.; Oliveira, O.N. TEM, XRD and AFM study of poly(o-ethoxyaniline) films: new evidence for the formation of conducting islands. *Appl. Phys. A* **2008**, *93*, 537, doi:10.1007/s00339-008-4686-9.

81. Bordin, E.R.; Frumi Camargo, A.; Rossetto, V.; Scapini, T.; Modkovski, T.A.; Weirich, S.; Carezia, C.; Barretta Franceschetti, M.; Balem, A.; Golunski, S.M.; et al. Non-Toxic Bioherbicides Obtained from Trichoderma koningiopsis Can Be Applied to the Control of Weeds in Agriculture Crops. *Ind. Biotechnol.* **2018**, *14*, 157–163, doi:10.1089/ind.2018.0007.

82. LEWIN, M.; GUTTMANN, H.; SAAR, N. New aspects of the accessibility of cellulose. In Proceedings of the Applied Polymer Symposium; Interscience, J.W., Ed.; New York, 1976; Vol. 28.

83. Yao, B.; Imani, F.; Sakpal, A.S.; Reutzel, E.W.; Yang, H. Multifractal Analysis of Image Profiles for the Characterization and Detection of Defects in Additive Manufacturing. *J. Manuf. Sci. Eng.* **2018**, *140*, doi:10.1115/1.4037891.

84. Chen, Y.; Yang, H. Numerical simulation and pattern characterization of nonlinear spatiotemporal dynamics on fractal surfaces for the whole-heart modeling applications. *Eur. Phys. J. B* **2016**, *89*, 181, doi:10.1140/epjb/e2016-60960-6.

85. Ţălu, Ş.; Stach, S.; Ghodselahi, T.; Ghaderi, A.; Solaymani, S.; Boochani, A.; Garczyk, Ż. Topographic Characterization of Cu–Ni NPs@a-C:H Films by AFM and Multifractal Analysis. *J. Phys. Chem. B* **2015**, *119*, 5662–5670, doi:10.1021/acs.jpcb.5b00042.

86. Ţălu, Ş.; Stach, S.; Mahajan, A.; Pathak, D.; Wagner, T.; Kumar, A.; Bedi, R.K.; Ţălu, M. Multifractal characterization of water soluble copper phthalocyanine based films surfaces. *Electron. Mater. Lett.* **2014**, *10*, 719–730, doi:10.1007/s13391-013-3270-4.

87. Ţălu, Ş. *Micro and nanoscale characterization of three dimensional surfaces*; Napoca Star Publishing House, Cluj-Napoca, Romania, 2015;

88. Ţălu, Ş.; Stach, S. Multifractal characterization of unworn hydrogel contact lens surfaces. *Polym. Eng. Sci.* **2014**, *54*, 1066–1080, doi:10.1002/pen.23650.

89. Ţălu, Ş.; Stach, S.; Valedbagi, S.; Bavadi, R.; Elahi, S.M.; Ţălu, M. Multifractal characteristics of titanium nitride thin films. *Mater. Sci.* **2015**, *33*, 541–548, doi:10.1515/msp-2015-0086.

90. Metz, G.; Ziliox, M.; Smith, S.O. Towards quantitative CP-MAS NMR. *Solid State Nucl. Magn. Reson.* **1996**, *7*, 155–160, doi:10.1016/S0926-2040(96)01257-X.

91. Sinha, N.; Grant, C. V.; Wu, C.H.; De Angelis, A.A.; Howell, S.C.; Opella, S.J. SPINAL modulated decoupling in high field double- and triple-resonance solid-state NMR experiments on stationary samples. *J. Magn. Reson.* **2005**, *177*, 197–202, doi:10.1016/j.jmr.2005.07.008.

92. Perdew, J.P. Density functional theory and the band gap problem. *Int. J. Quantum Chem.* **1985**, *28*, 497–523, doi:10.1002/qua.560280846.

93. Frisch, M. J.; Trucks, G. W.; Schlegel, H. B.; Scuseria, G. E.; Robb, M. A.; Cheeseman, J. R.; Montgomery, Jr., J. A.; Vreven, T.; Kudin, K. N.; Burant, J. C.; Millam, J. M.; Iyengar, S. S.; Tomasi, J.; Barone, V.; Mennucci, B.; Cossi, M.; Scalmani, G.; R, J.A. Gaussian 03 2004.

94. Perdew, J.P.; Burke, K.; Ernzerhof, M. Generalized gradient approximation made simple. *Phys. Rev. Lett.* **1996**, *77*, 3865–3868, doi:10.1103/PhysRevLett.77.3865.

95. Perdew, J.P.; Burke, K.; Ernzerhof, M. Generalized gradient approximation made simple [Phys. Rev. Lett. 77, 3865 (1996)]. *Phys. Rev. Lett.* **1997**, *78*, 1396–1396, doi:10.1103/PhysRevLett.78.1396.

96. Dennington, R.D.; Keith, T.A.; Millam, J.M. GaussView 2008.

97. Rosa, C. De; Auriemma, F. *Crystals and crystallinity in polymers: diffraction analysis of ordered and disordered crystals*; 1st ed.; John Wiley & Sons, Inc.: New Jersey, 2014; ISBN 1118690796.

98. Corradini, P.; Auriemma, F.; De Rosa, C. Crystals and crystallinity in polymeric materials. *Acc. Chem. Res.* **2006**, *39*, 314–323, doi:10.1021/ar040288n.

99. Canevarolo Jr., S. V. *Ciência dos polímeros. Um texto básico para tecnólogos e engenheiros*; 3rd ed.; Artiliber Editora Ltda: São Paulo, 2013;

100. Morales, G.M. Effects of high hydrochloric acid concentration on aniline chemical polymerization. *Polymer (Guildf).* **1997**, *38*, 5247–5250.

101. Chung, F.H.; Scott, R.W. A new approach to the determination of crystallinity of polymers by X-ray diffraction. *J. Appl. Crystallogr.* **1973**, *6*, 225–230, doi:10.1107/S0021889873008514.

102. Sanches, E.A.; Carolino, A.S.; Santos, A.L.; Fernandes, E.G.R.; Trichês, D.M.; Mascarenhas, Y.P. The use of Le Bail Method to analyze the semicrystalline pattern of a nanocomposite based on polyaniline emeraldine-salt form and α-Al2O3. *Adv. Mater. Sci. Eng.* **2015**, *2015*, 1–8.

103. Mazzeu, M.A.C.; Faria, L.K.; Cardoso, A. de M.; Gama, A.M.; Baldan, M.R.; Gonçalves, E.S. Structural and morphological characteristics of polyaniline synthesized in pilot scale. *J. Aerosp. Technol. Manag.* **2017**, *9*, 39–47, doi:10.5028/jatm.v9i1.726.

104. Stejskal, J.; Bober, P.; Trchová, M.; Nuzhnyy, D.; Bovtun, V.; Savinov, M.; Petzelt, J.; Proke, J. Interfaced conducting polymers. *Synth. Met.* **2017**, *224*, 109–115, doi:10.1016/j.synthmet.2016.12.029.

105. Bhadra, S.; Singha, N.K..; Khastgir, D. Effect of aromatic substitution in aniline on the properties of polyaniline. *Eur. Polym. J.* **2008**, *44*, 1763–1770.

106. Silva, A.S.; Soares, J.C.; Carolina, A.; Souza, S.M. De; Fernandes, E.G.R.; Mascarenhas, Y.P.; Sanches, E.A. Structural and morphological characterization of Poly(o-ethoxyaniline) Emeraldine-salt form using FTIR , XRD , LeBail Method and SEM. *J. Mol. Struct.* **2014**, doi:10.1016/j.molstruc.2014.04.039.

107. Trovati, G.; Sanches, E.A.; De Souza, S.M.; Dos Santos, A.L.; Neto, S.C.; Mascarenhas, Y.P.; Chierice, G.O. Rigid and semi rigid polyurethane resins: A structural investigation using DMA, SAXS and Le Bail method. *J. Mol. Struct.* **2014**, *1075*, 589–593, doi:10.1016/j.molstruc.2014.07.024.

108. Boutaleb, N.; Chouli, F.; Benyoucef, A.; Zeggai, F.Z.; Bachari, K. A comparative study on

surfactant cetyltrimethylammoniumbromide modified clay-based poly(p-anisidine) nanocomposites: Synthesis, characterization, optical and electrochemical properties. *Polym. Compos.* **2021**, *42*, 1648–1658, doi:10.1002/pc.25941.

109. Biondo, M.M.; Medeiros de Oliveira, L.; Lima, S.X.; Carolino, A. de S.; Farias Rocha, A.L.; da Silva, J.P.; Ruiz, Y.L.; Giacon, V.M.; Campelo, P.H.; Sanches, E.A. Chemically synthesized poly(o-methoxyaniline): Influence of counterions on the structural and electrical properties. *J. Mol. Struct.* **2020**, *1205*, 127588, doi:10.1016/j.molstruc.2019.127588.

110. Van Put, A.; Vertes, A.; Wegrzynek, D.; Treiger, B.; Van Grieken, R. Quantitative characterization of individual particle surfaces by fractal analysis of scanning electron microscope images. *Fresenius. J. Anal. Chem.* **1994**, *350*, 440–447, doi:10.1007/BF00321787.

111. Mannelquist, A.; Almqvist, N.; Fredriksson, S. Influence of tip geometry on fractal analysis of atomic force microscopy images. *Appl. Phys. A Mater. Sci. Process.* **1998**, *66*, S891–S895, doi:10.1007/s003390051262.

112. Fu, H.; Wang, W.; Chen, X.; Pia, G.; Li, J. Fractal and multifractal analysis of fracture surfaces caused by hydrogen embrittlement in high-Mn twinning/transformation-induced plasticity steels. *Appl. Surf. Sci.* **2019**, *470*, 870–881, doi:10.1016/j.apsusc.2018.11.179.

113. Nečas, D.; Klapetek, P. Gwyddion: An open-source software for SPM data analysis. *Cent. Eur. J. Phys.* 2012, *10*, 181–188.

114. Barabási, A.-L.; Vicsek, T. Multifractality of self-affine fractals. *Phys. Rev. A* **1991**, *44*, 2730–2733, doi:10.1103/PhysRevA.44.2730.

115. Grassberger, P.; Procaccia, I. Characterization of Strange Attractors. *Phys. Rev. Lett.* **1983**, *50*, 346–349, doi:10.1103/PhysRevLett.50.346.

116. Yadav, R.P.; Dwivedi, S.; Mittal, A.K.; Kumar, M.; Pandey, A.C. Fractal and multifractal analysis of LiF thin film surface. *Appl. Surf. Sci.* **2012**, *261*, 547–553, doi:10.1016/j.apsusc.2012.08.053.

117. Ghosh, K.; Pandey, R.K. Fractal and multifractal analysis of In-doped ZnO thin films deposited on glass, ITO, and silicon substrates. *Appl. Phys. A* **2019**, *125*, 98, doi:10.1007/s00339-019-2398-y.

118. Nasehnejad, M.; Gholipour Shahraki, M.; Nabiyouni, G. Atomic force microscopy study, kinetic roughening and multifractal analysis of electrodeposited silver films. *Appl. Surf. Sci.* **2016**, *389*, 735–741, doi:10.1016/j.apsusc.2016.07.134.

119. de Oliveira, L.M.; Matos, R.S.; Campelo, P.H.; Sanches, E.A.; da Fonseca Filho, H.D. Evaluation of the nanoscale surface applied to biodegradable nanoparticles containing Allium sativum essential oil. *Mater. Lett.* **2020**, *275*, 128111, doi:10.1016/j.matlet.2020.128111.

120. de Oliveira, L.M.; Matos, R.S.; Ţălu, Ş.; Rocha, A.L.F.; de Aguiar Nunes, R.Z.; Bezerra, J. de A.; Campelo Felix, P.H.; Inada, N.M.; Sanches, E.A.; da Fonseca Filho, H.D. Three-dimensional nanoscale morphological surface analysis of polymeric particles containing Allium sativum essential oil. *Materials (Basel).* **2022**, *15*, 2635, doi:10.3390/ma15072635.

121. da Silva, J.M.S.; de Souza Carolino, A.; de Oliveira, L.R.; de Souza Gonçalves, D.; Biondo,

M.M.; Campelo, P.H.; de Araújo Bezerra, J.; Ţălu, Ş.; da Fonseca Filho, H.D.; da Frota, H.O.; et al. Poly(o-methoxyaniline) Chain Degradation Based on a Heat Treatment (HT) Process: Combined Experimental and Theoretical Evaluation. *Molecules* **2022**, *27*, 3693, doi:10.3390/molecules27123693.

122. NIST NIST Standard Reference Data Program.

123. Reis, A.S.; Sanches, E.A.; Frota, H.O. Energy band structure and electronic transport properties of chlorine-doped polyaniline from ab initio calculations. *Synth. Met.* **2017**, *231*, 89–94, doi:10.1016/j.synthmet.2017.07.004.

124. Epstein, A.J.; Ginder, J.M.; Zuo, F.; Bigelow, R.W.; H.-S. Woo and D.B. Tanner; and A.F. Richter, W.-S.H. and A.G.M.D. Insulator To Metal Transition In Polyaniline. **1987**, *18*, 303–309.

125. Kang, E.T.; Neoh, K.G.; Tan, K.L. Polyaniline: A polymer with many interesting intrinsic redox states. *Prog. Polym. Sci.* **1998**, *23*, 277–324, doi:10.1016/S0079-6700(97)00030-0.

126. Kar, P. Influence of Properties of Conjugated Polymer on Doping. In *Doping in Conjugated Polymers*; John Wiley & Sons, Inc.: Hoboken, NJ, USA, 2013; pp. 81–96.

127. Boutaleb, N.; Chouli, F.; Benyoucef, A.; Zeggai, F.Z.; Bachari, K. A comparative study on surfactant etyltrimethylammoniumbromide modified clay-based poly(p-anisidine) nanocomposites: Synthesis, characterization, optical and electrochemical properties. *Polym. Compos.* **2021**, *42*, 1648–1658, doi:10.1002/pc.25941.

128. Hussin, H.; Gan, S.-N.; Phang, S.-W. Development of water-based polyaniline sensor for hydrazine detection. *Sensors Actuators A Phys.* **2021**, *317*, 112460, doi:10.1016/j.sna.2020.112460.

129. Bhadra, S.; Kim, N.H.; Rhee, K.Y.; Lee, J.H. Preparation of nanosize polyaniline by solid-state polymerization and determination of crystal structure. *Polym. Int.* **2009**, *58*, 1173–1180, doi:10.1002/pi.2646.

130. Ponder, J.F.; Gregory, S.A.; Atassi, A.; Menon, A.K.; Lang, A.W.; Savagian, L.R.; Reynolds, J.R.; Yee, S.K. Significant enhancement of the electrical conductivity of conjugated polymers by post-processing side chain removal. *J. Am. Chem. Soc.* **2022**, *144*, 1351–1360, doi:10.1021/jacs.1c11558.

131. Raghunathan, A.; Kahol, P.K.; McCormick, B.J. Electron localization in poly(alkoxyanilines). *Solid State Commun.* **1998**, *108*, 817–822, doi:10.1016/S0038-1098(98)00452-9.

132. Hassan, A.; Macedo, L.J.A.; Crespilho, F.N. Recognizing conductive islands in polymeric redox surfaces using electrochemical-coupled vibrational spectromicroscopy. *Chem. Commun.* **2020**, *56*, 10309–10312, doi:10.1039/D0CC03356A.

133. Nogueira, J.S.; Mattoso, L.H. c; Lepienski, C.M.; Faria, R.M. AC conduction of poly(o-methoxyaniline). *Synth. Met.* **1995**, *69*, 259–260, doi:10.1016/0379-6779(94)02440-A.

134. da Silva, L.S.; Biondo, M.M.; Feitosa, B. de A.; Rocha, A.L.F.; Pinto, C. da C.; Lima, S.X.; Nogueira, C. de L.; de Souza, S.M.; Ruiz, Y.L.; Campelo, P.H.; et al. Semiconducting nanocomposite based on the incorporation of polyaniline on the cellulose extracted from Bambusa vulgaris: structural, thermal and electrical properties. *Chem. Pap.* **2022**, *76*, 309–322, doi:10.1007/s11696-021-01844-z.

135. Nail;, G.H.; Mendel, T.A.J. Synthesis, characterization and study electrical conductivity of new Poly 4-methoxy aniline/manganese dioxide nano composite. *J. Educ. Sci. Stud. Chem.* **2021**, *17*, 65–73, doi:10.52866/esj.2021.05.17.05.